University of Bath

Alternative formats
If you require this document in an alternative format, please contact:
openaccess@bath.ac.uk

- A practical two parameter model of pile-soil gapping for prediction of monopile offshore wind turbine dynamics

Author 1
- Stephen A. Williams, MPhys (Hons)
- Department of Architecture and Civil Engineering, University of Bath, Claverton Down, Bath, BA2 7AY, UK
- https://orcid.org/0000-0002-1845-1462

Author 2
- Loizos Pelecanos, PhD
- Department of Architecture and Civil Engineering, University of Bath, Claverton Down, Bath, BA2 7AY, UK
- https://orcid.org/0000-0001-6183-1439

Author 3
- Antony P. Darby, PhD
- Department of Architecture and Civil Engineering, University of Bath, Claverton Down, Bath, BA2 7AY, UK

Full contact details of corresponding author.

- Stephen Williams, sw2007@bath.ac.uk, Department of Architecture and Civil Engineering, University of Bath, Claverton Down, Bath, BA2 7AY, UK

Abstract (150 – 200 words)

Monopile mounted offshore wind turbines (OWTs) are expected to experience a very large number of cyclic loads throughout their operational lifetime, and the existing *p-y* method of foundation modelling does not fully account for the effects of dynamic cyclic loading, such as pile-soil gapping. In this paper a dynamic model based on the beam-on-nonlinear-Winkler-foundation scheme with a novel algorithm capable of capturing the effects of pile-soil gapping is presented. It can account for gap cave in, and the resulting gap size can react dynamically to changing loading amplitudes, using only two calibration parameters. Static and dynamic cyclic loaded model validations are presented, and give very good agreement to experimental results, performing better than existing *p-y* curves for dynamic loading. The model is also applied to an OWT case study and predictions of natural frequency reduction due to soil erosion agree well with measured results. It is shown that the inclusion of gapping may result in a significant decrease to the natural frequency prediction of OWTs relative to the value predicted without gapping. As such, not considering gapping could lead to unconservative predictions, and any additional soil degradation throughout the serviceable lifetime could therefore result in unwanted resonance. The method provided in this paper provides a simple and accurate model to predict this behaviour which is crucial to ascertain during the design phase.

List of notations

α	mass damping coefficient
α_p	gap entry parameter
α_y	gap exit parameter
β	stiffness damping coefficient
κ	vertical capacity coefficient
v	soil Poisson ratio
ξ	target structural damping ratio
φ	angle of internal friction
ω	system circular frequency
ρ_s	density of soil
A	pile cross sectional area
a_0	dimensionless frequency
$[C]$	damping matrix
c_r	radiation damping coefficient

d_p	pile diameter
E_p	Youngs modulus of the pile
E_s	Youngs modulus of the soil
$\{F_{ext}\}$	external force vector
$\{F\}$	total force vector
f	applied load frequency
G_s	soil shear modulus
I_p	pile second moment of area
$[K]$	stiffness matrix
k_{max}	maximum soil spring stiffness
k_{spr}	spring stiffness
L_{EL}	element length
L_P	pile length
$[M]$	mass matrix
M_{RNA}	rotor-nacelle assembly mass
A	pile cross sectional area
N	load cycle number
N_p	earth pressure coefficient
n	Masing factor
P	lateral soil reaction force
P_{max}	ultimate capacity of lateral soil springs
P_r	soil reaction force upon reversal
p	distributed soil reaction force
p_{pos}	gap entry threshold for p decreasing
p_{neg}	gap entry threshold for p increasing
q	vertical soil reaction at base spring
r_p	pile radius
S_u	undrained shear strength of soil
T	vertical soil reaction force
T_{max}	ultimate capacity of vertical soil springs
t	time
V_s	shear wave velocity in soil
y	lateral displacement
y^N_{pos}	gap exit threshold for p increasing at cycle N
y^N_{neg}	gap exit threshold for p decreasing at cycle N
z	vertical displacement

1. Introduction

Offshore wind turbines (OWTs) are rapidly becoming a popular method of generating clean renewable electricity. The UK has already invested heavily in OWTs, with a total of £11.5bn to be invested by 2021 according to a report by the HM Treasury (2016). The majority of OWTs are constructed with monopile foundations, accounting for 80% of OWT installations as of December 2016 (Musial *et al.*, 2016).

Once operational, an OWT superstructure will be subjected to cyclic environmental loading mainly in the lateral direction from the wind and waves. A modern OWT is expected to remain serviceable for 25 - 30 years, and during that time it will experience millions, if not billions of cycles of loading (Lombardi *et al.*, 2013). Monopiles for use in OWTs are currently designed with a *beam-on-nonlinear-Winkler-foundation* (BNWF) type model using *p-y* and *T-z* curves recommended by DNV/Risø (2002) and the American Petroleum Institute, or API (2007). In this approach, sections of the pile are treated as discrete beam elements with soil reaction modelled using a set of mutually independent elastic, or elasto-plastic springs. The method is popular due to its simple implementation using prescribed *p-y* soil reaction curves for different foundation media. Current design specifications recommend cyclic loading curves based on empirical studies consisting of only hundreds of cycles (Achmus *et al.*, 2009). It has been extensively documented that continuous cyclic loading has an effect on the pile-soil interaction (Achmus *et al.*, 2009; Lombardi *et al.*, 2013; Yu *et al.*, 2015; Arshad & O'Kelly, 2016; Cui & Bhattacharya, 2016; Nikitas *et al.*, 2016), which in turn will affect the behaviour of the OWT superstructure. Damgaard *et al.* (2013) reported time-dependent natural frequencies for a selected OWT fitted with accelerometers and attributed this to the soil erosion in the top layers of the foundation & subsequent scour development. It is important then to be able to simulate and evaluate the effects of long-term cyclic loading on OWTs using the commonly used BNWF models.

The effect of cyclic loading is currently specified within the design codes simply as a reduction of the specified design capacity and a reduced soil stiffness in the p-y curves (API, 2007). However, it is not dependent on the number of cycles, the loading frequency, amplitude, or other dynamic parameters. One significant consequence of degradation within soils is the

31   formation of a gap between the upper layers of the soil and the pile due to plastic soil

32   deformation, known as gapping. Gapping causes unrestricted pile displacement and as such

33   affects the natural frequency of the laterally excited superstructure. It is an important effect to

34   include, as it has consequences both for cohesive and cohesionless soils. Either soil may

35   experience some cave in and gap closure, however for continuous cyclic loading the gap has

36   been shown to not cave in completely, even in cohesionless soils (Klinkvort, 2012).

37

38   OWTs experience loading from three main sources, environmental, self-weight, and rotor

39   loading. A typical spectrum of these excitation frequencies is displayed in Figure 1. The wind

40   and wave frequencies are dominant in the low frequency region, around 0.1 Hz. The rotor

41   loading, named 1P loading, references the frequency at which the turbine rotates, applying a

42   dynamic load to the structure within the operational frequency of the OWT rotor, typically

43   between 0.1 and 0.3 Hz. The 3P frequency represents the shadowing effect when a blade

44   passes in front of the tower, causing a wind deficiency that applies a load to the structure at

45   three times the 1P frequency for a three bladed turbine. The loading frequencies define three

46   structural design approaches, stiff-stiff, soft-stiff and soft-soft. The soft-soft regime uses the

47   least steel and as such has a natural frequency less than the 1P frequency. For modern large

48   turbines, the natural frequency would be too low and risk resonance with wind and wave

49   loading. The stiff-stiff regime has a natural frequency above 3P and is the safest design as it is

50   far removed from excitation frequencies but is not economically viable due to the large amount

51   of steel that would be required to ensure sufficient stiffness. The vast majority of modern OWTs

52   are therefore designed with a soft-stiff specification, meaning the natural frequency of the

53   superstructure lies between the 1P and the 3P frequencies (Lombardi *et al.*, 2013). This band of

54   stability is often narrow, especially once the regulatory allowances of ±5% above and below

55   each frequency band have been accounted for. If soil degradation in the upper layers of the

56   foundation causes a reduction in the natural frequency, it could lie within the 1P band of

57   resonance, requiring costly maintenance and possibly causing overturning failures due to

58   amplified dynamic response (Prendergast *et al.*, 2015). If the effect of gapping during long term

59   cyclic loading could be quantified prior to design, costs of developing overly stiff structures could

60   be reduced, and prevent over-conservative, expensive design.

62   Various computational models have been proposed to capture the gapping effect in dynamic

63   simulations. Boulanger *et al.* (1999) proposed a dynamic *p-y* method in which the nonlinear

64   curve consists of contributions from elastic, plastic, and gap components. The model was

65   validated against the results of seismic centrifuge tests. The model provided good agreement

66   with experimental results, however it is not capable of modelling soil cave-in. Taciroglu *et al.*

67   (2006) updated Boulanger's model to include a leading face, rear face and drag element, with a

68   more robust range of application for a range of soil and pile properties. However, neither model

69   is optimised for use in evaluating natural frequency, since the contributions of each spring

70   element in the overall soil stiffness is unclear, and calibrating the response is non-trivial

71   (Carswell *et al.*, 2016). For use in aiding OWT design, it is important that the effects of gapping

72   on the natural frequency can be quantified.

73

74   Klinkvort (2012) proposed a simple model to encapsulate this behaviour into a three-phase

75   approach, with each cycle consisting of nonlinear loading, elastic unloading and a gap phase.

76   However, the inclusion of linear unloading could cause overestimation of hysteretic damping,

77   and the model has not been validated for dynamic loading conditions.

78

79   Beuckelaers (2017) built upon the *PISA* project of Byrne *et al.* (2017) to include the effects of

80   gapping, based on a model proposed by Houlsby *et al.* (2005). It consists of a series of springs

81   and friction sliding elements. It is built within the *PISA* framework, so a 3D FE model is used to

82   derive *p-y* soil reaction curves, which are then implemented in a 1D model to test monopile

83   designs efficiently. It therefore avoids the use of traditional *p-y* curves. However, having only

84   been compared with the static *PISA* field tests, it has not yet been validated for use with

85   dynamic loading.

86

87   Presented here, is a proposed model based on a BNWF framework with a novel gapping

88   algorithm that can be calibrated with just two parameters. The model is designed to be simple to

89   calibrate and easily implemented into existing BNWF codes, and as such is advantageous to

90   design over similar models. It can be used to quickly and easily make a first prediction for

91   potential (adverse) gapping behaviour of monopile foundations. It is shown, through comparison

92   with static and dynamic cyclic loading tests of flexible and rigid piles, that the simple method can

93   reliably represent the gapping phenomena observed in experimental pile tests. The proposed

94   model is also compared with the existing *p-y* curves recommended by the API (2007) and is

95   shown to give better agreement with experimental results.

96

97   **2. The Model**

98

99   The model used in this study is based on a BNWF framework using Euler-Bernoulli beams and

100   a hyperbolic soil reaction curve, with a novel algorithm to simulate the pile-soil gapping.

101

102   ***2.1 Dynamic nonlinear p-y model***

103

104   A BNWF model concept was used, with *p-y, T-z* and *q-z* springs and viscous dampers used to

105   model the soil reaction. A schematic of the model concept applied to an OWT is displayed in

106   Figure 2, where M_{RNA} is the mass of the rotor-nacelle assembly atop the OWT tower, and *F* the

107   external applied force.

108

109   In order to avoid the documented discrepancies between the API (2007) *p-y* curves and

110   experimental results of both ultimate capacity (McGann *et al.,* 2011; Yoo *et al.,* 2013) and initial

111   stiffness (Boulanger *et al.,* 2003), as well as the exclusion of cyclic loading effects (Page *et al.,*

112   2017), the hyperbolic model of Duncan & Chang (1970) is used. The model is designed to be

113   flexible and compatible with additional soil degradation features, such as the decrease in

114   ultimate capacity seen in soils over large amplitude cyclic loading, i.e., cyclic strength

115   degradation (e.g., Poulos (1989), Chin & Poulos (1991) and others). This is not expected to be

116   an issue for application within OWT dynamics, since these structures are designed to

117   experience relatively small strain loads. If the existence of strain-softening is expected to be an

118   issue (i.e., decrease in the ultimate capacity and minor difference in damping), the hyperbolic

119   model can be modified (e.g., DHHM model of Pelecanos et al. (2018)) in order to account for

120   this while retaining compatibility with the gapping model. It is not considered in the following in

121   order to retain focus on the gapping mechanism and demonstrate calibration of the model

122   parameters independent of other soil degradation effects. The horizontal soil reaction in units of

123   N/m is calculated as

124

$$p = E_p I_p \frac{d^4 y}{dz^4}$$

125   (1)

126

127   where E_p and I_p are the Young's modulus and second moment of area of the structure

128   respectively. The derivative is of y, the lateral deflection in m, and z the depth from the pile head

129   in m.

130

131   The soil reaction curve, formulated using the hyperbolic model is given as

132

$$P = \frac{k_{max} \cdot y}{1 + y \cdot \frac{k_{max}}{P_{max}}}$$

133   (2)

134

135   where k_{max} is the maximum spring stiffness in N/m (so this can be implemented directly in a

136   code), and P is the reaction force in N. Masing (1926) rules

137   are implemented to model cyclic loading where, upon reversal, the backbone curve of Equation

138   2 takes the form

139

$$\frac{P - P_r}{n} = \frac{k_{max} \cdot \frac{y - y_r}{n}}{1 + \left| \frac{y - y_r}{n} \right| \frac{k_{max}}{P_{max}}}$$

140   (3)

141

142   where P_r and y_r are the values of reaction force and displacement upon reversal, and n is the

143   Masing factor by which the backbone curve is scaled, taken in this model to be $n = 1$ for virgin

144   loading, and $n = 2$ after the load reversal.

145

146 The k_{max} value used is that of Vesic (1961), as recommended in the study by Prendergast &

147 Gavin (2016) which found this coefficient to most closely model dynamic free vibration response

148 of monopiles. It is given in units of stiffness, i.e., N/m as

149

150
$$k_{max} = \frac{L_{EL} \cdot 0.65 \cdot E_s}{(1 - v^2)} \cdot \left(\frac{E_s \cdot d_p{}^4}{E_p \cdot I_p} \right)^{\frac{1}{12}} \tag{4}$$

151

152 where L_{EL} is the element length between Winkler springs in the BNWF model, E_s is the

153 measured Young's modulus and v the Poisson ratio of the soil, and d_p is the diameter of the pile.

154 The ultimate capacity of the pile is defined by the undrained shear strength of the soil, and is

155 given by Matlock, H. (1970) as

156

157 $P_{max} = L_{EL} \cdot N_p \cdot S_u \cdot d_p$ \hfill (5)

158

159 where N_p is the dimensionless earth pressure coefficient increasing with depth, linearly from a

160 value of 2 to a constant value of 11 from a depth of $z/d_p = 3$, and S_u is the undrained shear

161 strength of the soil. This relation is used to define the P_{max}, model parameter; any other relevant

162 relation (e.g., Broms(1964), Barton (1984), Reese & Welch (1975) or others) can be used.

163

164 The $T\text{-}z$ springs use the spring stiffness given by Randolph & Wroth (1978)

165

166
$$k_{max} = \pi \cdot d_p \cdot L_{EL} \cdot \frac{\frac{G_s}{d_p/2}}{ln \left(\frac{2.5 \cdot L_p \cdot (1-v)}{d_p/2} \right)}. \tag{6}$$

167

168 where G_s is the shear modulus of the soil and L_p is the total length of the pile. The value of T_{max}

169 is derived using

170

171 $T_{max} = \pi \cdot d_p \cdot L_{EL} \cdot \kappa \cdot S_u$ \hfill (7)

172

173 where κ is a coefficient derived depending on the nature of the soil and the pile installation

174 methods, commonly taken to be equal to 0.5. For the *q-z* spring the maximum stiffness value

175 from Boussinesq (1885) is used

176

177
$$k_{max} = \frac{2 \cdot d_p \cdot G_s}{1 - v} \qquad (8)$$

178

179 For this study, the gapping algorithm was not applied to the vertical *T-z* and *q-z* springs and, as

180 such, cyclic loading in the vertical direction is modelled simply with the Masing rules and the

181 hyperbolic model, with initial stiffness described by Equations 6 and 8 respectively, and with the

182 same ultimate capacity, given in Equation 7. Vertical gapping could be added with the same

183 rules as are described for the lateral springs. The elemental stiffness and mass system is

184 compiled into global stiffness and mass matrices, discretising the response into the second

185 order differential equation of motion (Bathe, 2006)

186

187
$$\{F\} = [M]\{\ddot{y}\} + [C]\{\dot{y}\} + [K]\{y\} \qquad (9)$$

188

189 where $\{F\}$ is the total force vector, $[M]$ is the mass matrix, $[C]$ the damping matrix and $[K]$ the

190 stiffness matrix of the global pile-soil system. Vectors of displacement, velocity, and acceleration

191 of each degree of freedom (DoF) throughout the time history are given by $\{y\}$, $\{\dot{y}\}$ and $\{\ddot{y}\}$

192 respectively.

193

194 The *p-y* spring stiffness used in Equation 9 is found by taking the derivative of Equation 3 with

195 respect to *y*, and then input to the relevant DoF in the stiffness matrix in Equation 9. The tangent

196 spring stiffness is therefore given by

197

198
$$k_{spr} = \frac{k_{max}}{\frac{k_{max}\left|\frac{y-y_r}{n}\right|}{P_{max}} + 1}$$
$$- \frac{k_{max}^2(y-y_r)^2}{n^2 P_{max}\left|\frac{y-y_r}{n}\right|\left(\frac{k_{max}\left|\frac{y-y_r}{n}\right|}{P_{max}} + 1\right)^2} \qquad (10)$$

200   in units of N/m. The two-dimensional elemental stiffness matrix used for the beam is the Euler-

201   Bernoulli formulation, which for the three DoFs of each node, axial/lateral displacement and

202   rotation, is given as seen in Equation 11, where A is the cross-sectional area of the pile. The

203   stiffness matrix in Equation 9 is then built from the elemental stiffness matrix [K_{EL}] and the

204   nonlinear stiffness of the p-y springs in Equation 10.

205

206

$$[K_{EL}] = \begin{pmatrix} \frac{E_p A}{L_{EL}} & 0 & 0 & -\frac{E_p A}{L_{EL}} & 0 & 0 \\ 0 & \frac{12 E_p I_p}{L_{EL}^3} & \frac{6 E_p I_p}{L_{EL}^2} & 0 & -\frac{12 E_p I_p}{L_{EL}^3} & \frac{6 E_p I_p}{L_{EL}^2} \\ 0 & \frac{6 E_p I_p}{L_{EL}^2} & \frac{4 E_p I_p}{L_{EL}} & 0 & -\frac{6 E_p I_p}{L_{EL}^2} & \frac{2 E_p I_p}{L_{EL}} \\ -\frac{E_p A}{L_{EL}} & 0 & 0 & \frac{E_p A}{L_{EL}} & 0 & 0 \\ 0 & -\frac{12 E_p I_p}{L_{EL}^3} & -\frac{6 E_p I_p}{L_{EL}^2} & 0 & \frac{12 E_p I_p}{L_{EL}^3} & -\frac{6 E_p I_p}{L_{EL}^2} \\ 0 & \frac{6 E_p I_p}{L_{EL}^2} & \frac{2 E_p I_p}{L_{EL}} & 0 & -\frac{6 E_p I_p}{L_{EL}^2} & \frac{4 E_p I_p}{L_{EL}} \end{pmatrix} \tag{11}$$

207

$$[M] = \frac{\rho A L_{EL}}{420} \begin{pmatrix} 140 & 0 & 0 & 70 & 0 & 0 \\ 0 & 156 & 22 L_{EL} & 0 & 54 & -13 L_{EL} \\ 0 & 22 L_{EL} & 4 L_{EL}^2 & 0 & 13 L_{EL} & -3 L_{EL}^2 \\ 70 & 0 & 0 & 140 & 0 & 0 \\ 0 & 54 & 13 L_{EL} & 0 & 156 & -22 L_{EL} \\ 0 & -13 L_{EL} & -3 L_{EL}^2 & 0 & -22 L_{EL} & 4 L_{EL}^2 \end{pmatrix} \tag{12}$$

208

209

210   Mass is modelled using the elemental mass matrix in Equation 12, where ρ is the mass density

211   of the pile. Any concentrated masses such as the mass of the nacelle of an OWT, M_{RNA} seen in

212   Figure 2, are added to the nodal mass on the diagonal of the [M] matrix.

213

214   The equation of motion in Equation 9 is solved implicitly and incrementally, using the Newmark

215   beta method (Newmark, 1959) and tangent stiffness iterative solver. Using this method,

216   Equation 9 becomes

217

$$\left[\frac{1}{\beta \Delta t^2}[M] + \frac{\gamma}{\beta \Delta t}[C] + [K] \right] \{\Delta y_t\} =$$
$$\{\Delta F^{ext}\} + [M] \left[\frac{1}{\beta \Delta t}\{\dot{y}_{t-\Delta t}\} + \frac{1}{2\beta}\{\ddot{y}_{t-\Delta t}\} \right]$$
$$+ [C] \left[\frac{\gamma}{\beta}\{\dot{y}_{t-\Delta t}\} + \Delta t \left(\frac{\gamma}{2\beta} - 1 \right) \{\ddot{y}_{t-\Delta t}\} \right] \tag{13}$$

218

219

220 where $\{\Delta F^{ext}\}$ is the increment of externally applied force and Δt is the timestep. Sensitivity

221 analyses were performed to ensure small enough timesteps to give a solution with minimal

222 numerical error and a good performance time. For the analyses in this study, loading cycles

223 were divided into 800 timesteps to ensure convergence, as it was found, via a sensitivity study,

224 to be an acceptable balance between minimising numerical error and maintaining efficient

225 computation times. This value is likely conservative, and could be reduced for studies involving

226 long term loading and hundreds of cycles to reduce computation time. Values of the dissipative

227 version of the method with $\gamma = 0.6$ and $\beta = 0.3025$ were used in the Newmark scheme so as to

228 filter out high frequency noise that can be present when using the more traditional constant

229 acceleration values of $\gamma = 0.5$ and $\beta = 0.25$.

230

231 *2.2 Damping*

232

233 The total damping present in the system consists of contributions from structural, hysteretic and

234 radiation sources. Structural damping is modelled as modal Rayleigh damping and, as such, the

235 damping matrix $[C]$ is expressed as a linear combination of the mass and stiffness matrices

236

237 $\quad [C] = \alpha[M] + \beta[K]$ (14)

238

239 where the classical damping formulations are used

240

241 $$\alpha = \frac{2\xi\omega_1\omega_2}{(\omega_1 + \omega_2)}$$ (15)

242 $$\beta = \frac{2\xi}{(\omega_1 + \omega_2)}$$ (16)

243

244 where ω_1 and ω_2 are the first and third circular frequencies of the system, determined with an

245 eigenvalue analysis. Alternatively, for a dynamically driven system, undergoing periodic

246 excitation, one of the representative frequencies used in Equations 15 and 16 can be the driving

247   frequency of the externally applied force. The coefficient ξ is defined to specify the damping

248   ratio of the system, generally taken between 5% and 8% for embedded monopile foundations,

249   and between 0.5% and 1.5% for an OWT (Shirzadeh *et al.*, 2013). The coefficient ξ is assumed

250   to be equal for both representative frequencies ω_1 and ω_2, as the model was found to be

251   insensitive to independent target damping values. The target damping in this study was set to

252   1% for the OWT model, and at 5% for the embedded monopile tests.

253

254   Hysteretic damping is intrinsically included within the hyperbolic model of soil response due to

255   the adoption of Masing rules, and can be calculated as the ratio between the area of the force-

256   displacement loop, to the area bound by the secant stiffness at maximum displacement.

257   The radiation damping is modelled by including a viscous dashpot in parallel with *p-y* springs, as

258   seen in Figure 2. This accounts for the energy dissipated into the surrounding soil during

259   dynamic cyclic loading via the transmitted stress waves. The damping coefficient, c_r, used was

260   that of Gazetas & Dobry (1984) and is formulated as

261

$$\frac{c_r}{2d_p\rho_s V_s} = \left[1 + \left(\frac{3.4}{\pi(1-v)}\right)^{5/4}\right]\left(\frac{\pi}{4}\right)^{3/4} a_0^{-1/4} \quad (17)$$

262

263

264   where V_s is the shear wave velocity in the soil, ρ_s is the mass density of the soil, and $a_0 =$

265   $2\pi f d_p / V_s$ is the dimensionless frequency. Here *f* is the frequency of the applied load. The value

266   of c_r is tuned via a multiplicative coefficient to achieve the required amount of foundation

267   damping, estimated to be 0.5% for an OWT monopile in this study, to allow for a total damping

268   of 1.5%, which is informed from the findings of Shirzadeh *et al.* (2013).

269

270   ***2.3 Gapping rules***

271

272   The gapping model is based on a set of threshold values of *p* and *y* that correspond to entering

273   and exiting the gap phase of motion. The model is based on the three-phase approach of

274   Klinkvort (2012), with parameters defined to model changing soil condition such as cave-in

275   depending on the cohesiveness and properties of the soil. If a node does not enter those

276   threshold values, it will simply follow the Masing rules and hyperbolic *p-y* curve, only affected

277   inertially by other nodes in gap phases. When a node is in the gap phase, the only resistance to

278   motion experienced originates from the side shear friction acting on the pile. The node will

279   continue moving in the gap phase until it meets the opposite side of the soil and experiences the

280   hyperbolic resistance curve again, with a Masing factor set to $n = 1$, becoming $n = 2$ as usual

281   upon reversal.

282

283   An example schematic of cyclic loading and gap formation *p-y* curve is displayed in Figure 3.

284   The model is based upon two gapping parameters, a threshold in *p* for entering the gap, p_{pos}

285   and p_{neg} for decreasing and increasing *p* respectively, and a threshold in *y* for exiting the gap,

286   y_{neg} and y_{pos} for *y* decreasing and increasing respectively. A node will enter the gap if its *p* value

287   crosses the threshold defined by

288

289   $$p_{pos} = \alpha_p(z)\lceil p \rceil \qquad (18)$$

290   $$p_{neg} = \alpha_p(z)\lfloor p \rfloor \qquad (19)$$

291

292   where $\lfloor p \rfloor$ is the minimum and $\lceil p \rceil$ the maximum *p* value for that DoF over the loading time

293   history so far. The parameter $\alpha_p(z)$ is a calibrated factor that controls the depth to which gapping

294   occurs. The closer to 1 the parameter is, the more time that DoF will spend in the gap in a

295   particular cycle, and the smaller it is, the less time will be spent in the gap. This behaviour is

296   displayed in Figure 4, where an example dynamic *p-y* curve at ground level ($z = 0$) is shown for

297   values of $\alpha_p(0)$ from -0.1 to 0.1. If the value of $\alpha_p(z)$ becomes negative enough, that DoF will not

298   experience *p* values small/large enough to cross the threshold and enter the gap. This is used

299   as a proxy for an assigned critical gapping depth, motivated by experimental results that claim

300   gapping will occur to depths of approximately half the embedded length of the pile (Taborda *et*

301   *al.*, 2019; Byrne *et al.*, 2019) for rigid piles. The $\alpha_p(z)$ parameter is tuned as a function of depth

302   to enforce this critical depth within the model. The gradient to which this value decreases with

303   depth can be calibrated to experimental pile test results.

304

305   If the node enters the gap, it will continue until the y value equals the threshold in displacement

306   y_{neg}^{N} or y_{pos}^{N}. The index N is the load cycle number, where values are indexed because the gap

307   exit value of one cycle in one direction is dependent on the entry value of the previous cycle in

308   the opposite direction. The threshold values are given by

309

310    $$y_{neg}^{N} = \begin{cases} \alpha_y \lfloor y \rfloor & \text{if } y \leq 0 \ \ N = 1 \\ \alpha_y y_{neg,entry}^{N-1} & \text{if } y \leq 0 \ \ N > 1 \end{cases} \qquad (20)$$

311    $$y_{pos}^{N} = \begin{cases} \alpha_y \lceil y \rceil & \text{if } y \geq 0 \ \ N = 1 \\ \alpha_y y_{pos,entry}^{N-1} & \text{if } y \geq 0 \ \ N > 1 \end{cases} \qquad (21)$$

312

313   where $\lfloor y \rfloor$ is the minimum and $\lceil y \rceil$ the maximum y value for that DoF over the time history of

314   loading. As is displayed in Figure 3, the values of $y_{neg,entry}{}^{N-1}$ and $y_{pos,entry}{}^{N-1}$ are saved upon entry

315   of the gap for p increasing and decreasing respectively. The exit thresholds $y_{neg}{}^{N}$ and $y_{pos}{}^{N}$ are

316   then derived from these values, assuming $N > 1$. If it is the first cycle of loading, these values

317   are derived from the maximum and minimum y values so far. The gapping thresholds are

318   defined as such to allow for dynamic behaviour, where the gap size can respond to changing

319   loading conditions. The second gapping parameter, α_y, has a value between 0 and 1 and acts as

320   a cave in parameter. A value of α_y closer to 0 means the gap will readily cave in, and only a

321   fraction of the gap will remain after the pile has exited the gap. An analysis of the α_y parameter

322   is shown in Figure 5, showing example results of the p-y curve of a dynamically loaded pile at

323   ground level. The α_y parameter is set at 0.0 - 1.0 in intervals of 0.25. It is observed that the

324   gapping effect increases with α_y, where for a value of 1.0 that node is almost within the gap for

325   the entire load cycle. It is also clear that the secant stiffness of the soil response decreases

326   significantly for increasing α_y. As a further example, in the schematic in Figure 3, the gapping

327   parameters are approximately $\alpha_y \sim 0.5$ and $\alpha_p \sim 0.1$.

328

329   When the pile is in the gap phase, the radiation damping contribution from that node is reduced

330   to zero, and the spring constant is reduced to some fraction of the k_{max} value given in Equation

331   4. For all the following analyses, 5% of k_{max} was used as the resistance within the gap. Using

332   these simple rules, the gapping model can be easily implemented into existing static and

333   dynamic BNWF codes.

334

335   *2.4 Calibration*

336

337   The two parameters of the gapping model would be challenging to define strictly analytically.

338   However, they relate to physical properties of the soil medium and as such can be estimated,

339   using some engineering judgement, based on the tests outlined in this study. If detailed soil

340   information or monitored *p-y* curves are available, the gapping parameters can be back-

341   calculated simply; if not, parameters can be estimated to give a first estimate of potential

342   gapping behaviour. The case studies investigated in this report are listed in Table 1, as well as

343   the soil type, and gapping parameters used. The first gapping parameter, α_y, is a control of how

344   stable the gap will be under repeated cyclic loading. It is seen from Table 1 that the tests of

345   Rosquoet (2004) and Ting (1987), performed in dry sand and silty soil, will be expected to have

346   a low cohesion, and as such, will have an unstable gap that will easily cave in. The other two

347   tests were in dense marine sand and dense sand with layers of firm clay, which would be

348   expected to have a better gap stability. As such, the α_y value for the first two tests is lower than

349   the tests in the more cohesive soil. This parameter can, therefore, be estimated from basic soil

350   properties. The second parameter, α_p, effectively controls the depth to which the gap is active

351   down the pile. All four tests have α_p values within a small range, with the flexible piles having a

352   smaller initial α_p value, due to the fact the gap is active over a smaller fraction of the total pile

353   length, relative to the rigid piles. As such, an initial value of this parameter can be ascertained

354   from the geometric properties of the pile, and then tuned with depth by using the same gradient

355   with normalised depth as one of the example calibrations in Table 1 to obtain a realistic active

356   depth of gapping down the pile. As can be seen in Figure 4, the pile response is not as sensitive

357   to the α_p parameter, and so the initial choice for this value will not drastically alter the gapping

358   prediction. In all case studies considered in this work the calibration was based on the

359   minimization of the difference of the p-y loop values between the observed test data and the

360   model predictions (e.g., see Figures 8, 10, 14).

361 It is recognised that gapping may still be a new concept in OWT pile modelling and therefore not

362 many relevant tests have been conducted yet, which can provide relevant data that are useful

363 for calibrating the model. It is however, expected that more such tests will be performed and

364 published in the coming years and therefore a relevant database of useful data will be

365 developed that can hopefully be used to identify patterns in the data and define these

366 parameters with less uncertainty. It is therefore suggested, in the absence of a sufficient number

367 of available field tests (and relevant data) at the moment, that researchers use the

368 (representative) parameters back-calculated from this study (Table 1), as these appear to fall

369 within a rather narrow range.

370

371 Table 1. Details of the case studies examined in this report, and the gapping parameters used

372 to model them.

Case study reference	Soil type	L_p/d_p	α_y	$\alpha_P(z)$	α_P values (range)
PISA [Byrne *et al.* (2017)]	Dense marine sand	5.25 (rigid)	0.5	$0.2 - 0.2z$	0.2 to -0.6
Rosquoet (2004)	Dry fontainebleu sand	16.67 (flexible)	0.35	$0.05 - 0.095z$	0.05 to -0.3
Ting (1987)	Silty soil	15.98 (flexible)	0.35	$0.1 - 0.085z$	0.1 to -0.7
Kentish Flats OWT	Dense sand & firm clay	6.86 (rigid)	0.65	$0.2 - 0.027z$	0.2 to –0.6

373

374 **3. Model Validations**

375

376 A series of validations of the gapping models behaviour under static monotonic, cyclic and

377 dynamic cyclic loading regimes are presented. Results are compared to those calculated using

378 the recommended API (2007) curves and the Boulanger *et al.* (1999) model of gapping.

379 Analysis for the proposed model was performed entirely in MATLAB, and OpenSEES software

380 (Mazzoni *et al.*, 2006) was used for the comparisons to API curves, using the *PySimple1*

381   material for soil reaction. This material model was selected as it is an implementation of the

382   Boulanger gapping model into the OpenSEES framework, with *soilType* set to 2, for the API

383   sand relation, the drag resistance term was set to 0.1, back calculated from the pile tests that

384   were modelled. The parameters were selected to as closely resemble to presented model to

385   allow for comparison.

386

387   Pile geometry and soil characteristic values are taken from experimental records. The two

388   gapping parameters were selected to calibrate the features of the modelled *p-y* curves with the

389   curves given in experimental data, often at multiple depths down the pile. In the cases that a

390   model was loaded cyclically, it was simulated until steady state behaviour was reached, and the

391   steady state *p-y* curves were used to compare with experimental results.

392

393   A sensitivity study was performed for the length of beam elements in the model. A dynamic

394   pushover test was simulated with increasingly fine mesh cases, and a satisfactory convergence

395   was found for element lengths of 0.1 m and less. Figure 6 shows the maximum pile

396   displacement at ground level for an example pile of 10 m length and 0.61 m diameter for each

397   element length. As such, the element length of 0.1 m, or 100 elements in this case, was used in

398   the subsequent models as a satisfactory mesh density for the pile tests.

399

400   ***3.1 Static monotonic loading***

401

402   The proposed model is calibrated to a static monotonic load test to validate the use of the Euler-

403   Bernoulli beam model and hyperbolic soil reaction curves with the equations described in the

404   previous section for a laterally loaded monopile. The full-scale pile test by Huang *et al.* (2001)

405   was used as an experimental validation. The pile was 35 m long with a 1.5 m diameter, and the

406   soil shear modulus was modelled to increase with depth with a gradient of 9.5 MPa/m from a

407   value of 77 MPa at ground level. The pile was loaded monotonically to a maximum force of 3

408   MN, as in the experiment.

409

410   The force-displacement curve at the pile head is compared with experimental results in Figure

411   7, and gives good agreement, justifying the use of the hyperbolic model and the subgrade

412   modulus expression given in Equation 4, as well as the use of Euler-Bernoulli beams to model

413   the pile.

414

415   ***3.2 Static cyclic loading***

416

417   The *PISA* project of Byrne *et al.* (2017) performed a series of static lateral load tests on full

418   scale monopiles. Experimental data of a static cyclic load test from the project detailed in

419   Beuckelaers (2017) was used for validation of the gapping algorithm applied to a rigid pile

420   undergoing static cyclic loading. The steel pile had a 0.762 m outer diameter, 14 mm wall

421   thickness and a 4 m embedded depth. The loading is applied from the top of a 10 m stick-up

422   above ground. This gives the pile an embedded L_p/d_p ratio of 5.25, which would be expected to

423   exhibit rigid behaviour (LeBlanc *et al.*, 2010). The pile was embedded in sand, the shear

424   modulus of which is given in Beuckelaers (2017) from CPT data and was modelled to vary with

425   depth from 10 MPa at ground level to 175 MPa at the pile toe. The pile is loaded sinusoidally

426   from the top node at a frequency of 0.015 Hz with a peak applied force of 30 kN. The gapping

427   parameters were calibrated to have values of $α_y = 0.5$ while $α_p(z)$ varied linearly with depth from

428   0.2 at the ground level to -0.6 at the pile toe. The results of the cyclic loading are displayed in

429   Figure 8.

430

431   The modelled *p-y* curves are compared to experimental data, as well as the results given by the

432   Boulanger *et al.* (1999) gapping model with API recommended *p-y* curves for sand, taken at

433   depths below ground level of 0.5 m, 1.5 m and 3.5 m. The results, displayed in Figure 8, give

434   reasonable agreement for all three recorded depths, with slight overestimations of displacement

435   at all depths. The accuracy of the modelled response decreases with depth down the pile, with

436   the damping underestimated for the deeper simulations, and it appears that experimental data

437   at higher depths is less reliable as the observed behaviour follows a "quasi-linear" response

438   (Beuckelaers, 2017). The proposed model reproduces the area of the *p-y* curves well, as seen

439   in Figure 8d, and as such models well the damping present in the system. It is seen that the API

440   curves and Boulanger model significantly overestimates the loop area in the upper soil layers,

441   and underestimates at greater depths, predicting no non-linear behaviour at 3.5 m below the

442   ground level.

443

444   Figure 9 displays the profile of maximum and minimum displacement and gap size throughout

445   the cyclic loading. It is observed that significant gapping behaviour occurs down to

446   approximately 2 m below ground level, which is half the embedded depth.

447

448   Rosquoet (2004) carried out a series of cyclically loaded centrifuge tests on a model aluminium

449   pile with prototype dimensions of 12 m embedded depth, 0.72 m diameter and a 2.6 m stick-up.

450   It was embedded into dry Fontainebleu sand, modelled with a shear modulus increasing from 10

451   MPa to 120 MPa at the pile toe, loaded statically. The experimental test P330 has been

452   simulated, in which the pile was loaded at an amplitude of 0.960 MN at a frequency of 0.143 Hz.

453   The opening of a gap was modelled with parameters calibrated to the experimental *p-y* curve as

454     $\alpha_y = 0.35$ and $\alpha_p(z)$ varying from 0.05 to -0.3 with depth.

455

456   Results of the force-displacement curve at the pile head are presented in Figure 10a, and

457   compared with experimental values as well as the results of a 3D FE model proposed by Sheil &

458   McCabe (2017), to compare the performance of this 1D model with that of a 3D model. It is

459   noted that the experimental model has experienced ratcheting, as the *P-y* curve has undergone

460   a translation from being centred on the origin and has experienced some degree of stiffening.

461   The model presented in this study does not consider the effect of ratcheting, so this is not

462   captured in the modelled output. Profiles of the bending moment with depth as well as the soil

463   reaction force are also compared with experimental measurements in Figure 10b and 10c. The

464   proposed model shows good agreement with experimental results, and the ability to reproduce

465   the gapping effect as capable as a more computationally expensive 3D model.

466

467   ***3.3 Dynamic cyclic loading***

468

469 Dynamic full scale cyclic load tests are scarcely performed in the literature, due to the great

470 expense of a load setup capable of dynamic motions, as well as the fact that experimental full

471 scale tests have traditionally been motivated by building foundations, where dynamic cyclic

472 loading is not expected be a concern. For OWTs however, the environmental and rotor loading

473 are cyclic and dynamic in nature and so the performance of monopile foundations needs to be

474 adequately modelled. A full-scale test performed by Ting (1987) was selected to compare the

475 model to. A 12.2 m long steel pile was embedded 9.75 m into silty soil and loaded dynamically

476 at the top of the 2.45 m stick-up. It had a diameter of 0.61 m and a 13 mm wall thickness. The

477 soil Young's modulus is modelled to increase linearly from 10 MPa at the pile head to 55 MPa at

478 the pile tip. The undrained shear strength of the soil has an average value of 25 kPa. The mass

479 of the loading device was modelled with a 25-tonne point mass applied at 0.93 m from the top of

480 the pile. A static pushover was performed in both models to calibrate the response of the API

481 curves, and a good match of initial stiffness behaviour was found for angle of internal friction of

482 $\varphi = 29°$. The pile was loaded at a frequency of 2.09 Hz at an amplitude of 22 kN. Eigenvalue

483 analysis in MATLAB, using the inbuilt function *eig*, gives the natural frequency of the structure to

484 be 2.05 Hz, so this loading is considered as dynamic, such that inertial effects become

485 important. The gapping parameters used were $\alpha_y = 0.35$ and $\alpha_p(z)$ decreased linearly with depth

486 from 0.1 at ground level to -0.7 at the pile toe.

487

488 Profiles of deflection, soil reaction and moment are plotted in Figures 11 - 13 and compared to

489 experimental results. It is not stated in the report at which timesteps these profiles were

490 measured, so results were taken at 7 evenly spaced timesteps during the final cycle of loading.

491 These were used for a qualitative comparison of the magnitude and the shape of the profiles.

492 The resulting *p-y* curves for depths 1 - 6 pile diameters of the proposed model are displayed in

493 Figure 14a and the results of the API curves and Boulanger model in Figure 14b. Experimental

494 *p-y* curves for comparison are displayed in Figure 14c.

495

496 The results of the proposed model give good agreement to experimental results and reproduce

497 the gapping effect well. Maximum values of *p* and *y* are reproduced well, and the initially

498 increasing maximum *p* value with depth is also recreated. Comparing the profiles in Figures 11 -

499   13, the results from the proposed model more accurately qualitatively reflect those of the

500   experiment, compared to the API curve results. As seen in Figure 14, the API curves and

501   Boulanger model also do not as accurately model the gapping effect and like the results of the

502   static cyclic loading test in Figure 8d, underestimate the damping at greater depths.

503

504   **4. Application to an OWT case study**

505

506   In the study by Damgaard *et al.* (2013), an OWT was fitted with accelerometers and the natural

507   frequency measured with rotor stop tests over a series of weeks. It was found that the natural

508   frequency of the installed V90 3.0 MW OWT in Kentish Flats wind farm had varied between

509   0.340 Hz to approximately 0.327 Hz from measurements when tide and wind speed were

510   consistent to ensure similar external load prior to the rotor stop. The reduction in natural

511   frequency was likely attributed to soil degradation around the pile head from continual cyclic

512   loading (Damgaard *et al.*, 2013).

513

514   Geometric specifications of the OWT were taken from Amar Bouzid *et al.* (2018), and the OWT

515   was modelled as a 105.56 m superstructure, of which 29.5 m is the embedded monopile, 16 m

516   is the transition piece connecting the foundation to the 60.06 m tall tower. The monopile and

517   transition piece have a diameter of 4.3 m, while the towers diameter is modelled to vary linearly

518   with length from 2.3 m at the top to 4.45 m at the transition piece. The nacelle was modelled as

519   a point mass on the top node, with a mass of 130800 kg. Aerodynamic damping was not

520   considered in this simulation, since during the rotor stop tests once the blades have been

521   feathered aerodynamic damping would not be significant (Shirzadeh *et al.*, 2013). Equally, the

522   hydrodynamic damping has not been considered in this simulation (as its magnitude is

523   significantly smaller), in order to keep the focus on the soil-structure interaction and the soil

524   contribution to the damping. However, it could be included with the addition of viscous dampers

525   along depth of the water. The pile is embedded in layers of dense sand and firm clay and was

526   modelled with an average shear modulus of 60 MPa (Amar Bouzid *et al.*, 2018).

527

528   The model was loaded sinuisoidally for 20 periods (Figure 17), or 100 seconds, then allowed to

529   freely vibrate for 200 seconds. The gapping algorithm was calibrated with parameters $\alpha_y = 0.65$

530   and $\alpha_p = 0.2$ decreasing linearly to -0.6 at the pile toe. The α_y value was informed by the

531   previously mentioned calibrations, with a slightly higher value to reflect the higher density of the

532   sand and presence of stiff clay, reflecting a more cohesive soil. The value of α_p reflected that of

533   the calibration of the rigid pile test by Byrne *et al.* (2017) since this pile has a similar length to

534   diameter ratio and was calibrated to have the same gradient of $\alpha_p(z)$ with normalised

535   embedment depth.

536

537   A fast Fourier analysis was performed in Matlab using the *fft* function on the free vibration

538   portion of the time history, from 100 seconds onward, to assess the natural frequency of the

539   OWT. It was found that the gapping behaviour resulted in a reduction of natural frequency, as

540   displayed in Figure 15. The natural frequency calculated was 0.338 Hz without gapping, and

541   0.327 Hz with gapping, agreeing with the reduction recorded in the experimental data of

542   Damgaard *et al.* (2013), and the gap depth was observed to be approximately 9 m, as shown in

543   Figure 16. This suggests gapping behaviour to depths of the order of 0.30 L_p. Figure 15 also

544   shows the 1P frequency, which has a value of 0.3255 Hz, meaning the gapping behaviour

545   causes the OWT to have a natural frequency just inside the serviceable limit. A gapping effect

546   any more severe would cause the OWT to enter this 1P resonance limit, and could cause

547   significant damage to the structure, or failure. Additionally, a series of time-domain analyses has

548   been performed where the input frequency of the applied load was changed with respect to the

549   fundamental frequency of the OWT (without gapping) for cases considering and ignoring

550   damping. Figure 16 shows the maximum acceleration at the top of the OWT against the ratio of

551   the normalised input frequency for the cases with and without gapping and it is clearly shown

552   that the former case is associated with a smaller fundamental frequency, about 4% smaller than

553   the corresponding no-gapping case.

554

555   Where the gap which forms is a significant percentage of the maximum deflection of the pile

556   head, this can be considered scour, since the pile would experience little to no resistance from

557   the soil at the extrema of its deflection, so the soil could be considered to have completely

558   eroded. Scour can be modelled simply by reducing the embedment of a Winkler model.

559   However, this does not include the effects of gapping beneath the scour limit where the gap

560   created is not as significant a fraction of the displacement extrema. Damgaard *et al.* (2013)

561   found, using a Winkler model, that for a scour depth of 3 m, a natural frequency of 0.327 Hz is

562   measured. However, using this gapping model, if scour is considered as when the gap width is

563   ≥ 90% of maximum deflection, then the scour depth measured in this simulation is only 1.5 m for

564   the same reduction in natural frequency. So, by considering the additional effect of gapping

565   beneath the scour depth, the natural frequency reduction could be greater than expected if only

566   considering scour.

567

568   **5. Conclusions**

569

570   To avoid the economic drawbacks of over conservatism in design, the long-term behaviour of

571   OWTs must be evaluated prior to installation. A new dynamic Winkler model of an OWT capable

572   of considering the effect of soil degradation and gapping has been developed. The model has

573   been validated against static monotonic, cyclic, and dynamic cyclic pile tests, as well as rotor

574   stop tests performed on an operational OWT. It is concluded that the model reproduces the

575   dynamic pile-soil interaction very well and can predict the resulting effect on OWT natural

576   frequency. The model is easily calibrated, and controlled with only two parameters, α_y and α_p.

577   These can be estimated using available experimental *p-y* curves from dynamic pile tests

578   performed on site, or from tests in similar soil conditions, and are motivated by physical

579   properties of the soil and pile. From the results of the gapping algorithm applied to the OWT

580   model, the decrease in natural frequency observed in experimental results is reproduced well.

581

582   The model presented is capable of modelling gapping for unidirectional static and dynamic

583   loading, and this approach can be extended to multidirectional loading, of particular importance

584   for OWTs due to the out of phase loading of wind and waves. Additionally, this approach can be

585   applied to more realistic stochastic load conditions representative of the environmental forces

586   an OWT would be subjected to during the operational lifetime, and aid design accordingly. Due

587   to the simplicity of the model and its compatibility with BNWF methods, it can be used with

588 existing design techniques to improve predictions of OWT natural frequency and can be tested

589 exhaustively and efficiently over a variety of load conditions, soil conditions and structural

590 geometries. It will also be useful for other applications of piles under long-term sustained cyclic

591 load, such as other offshore structures (e.g., oil rig platforms, piles used for anchoring mooring

592 structures etc.) or foundations of structures experiencing high wind loads (e.g., power supply

593 pylons).

594

595 The results of this study encourage additional research on OWT dynamics, and how prediction

596 of natural frequency reduction is required to acquire a complete picture of how soil degradation

597 effects OWT behaviour. Particularly with the rapid development of larger and more rigid

598 foundations, these mechanisms need to be considered during the design phase. It is shown that

599 development and exploration of models of dynamic cyclic pile-soil interaction should be a

600 priority since the degradation of soil around an OWT foundation can have a profound impact on

601 its safety of operation.

602

606

607 **References**

608

609 Achmus, M., Kuo, Y. S. & Abdel-Rahman, K. (2009). Behavior of monopile foundations under

610 cyclic lateral load. *Computers and Geotechnics* 36, No. 5, 725–735,

611 doi:10.1016/j.compgeo.2008.12. 003.

612 Amar Bouzid, D., Bhattacharya, S. & Otsmane, L. (2018). Assessment of natural frequency of

613 installed offshore wind turbines using nonlinear finite element model considering soilmonopile

614 interaction. *Journal of Rock Mechanics and Geotechnical Engineering* 10, No. 2, 333–346,

615 doi:10.1016/j.jrmge.2017.11.010.

616   API (2007). API RP 2A - Recommended Practice for Planning, Designing and Constructing

617   Fixed Offshore Platforms — Working Stress Design. *API Recommended Practice*

618   doi:10.1007/ s13398-014-0173-7.2.

619   Arshad, M. & O'Kelly, B. C. (2016). Analysis and Design of Monopile Foundations for Offshore

620   Wind-Turbine Structures. *Marine Georesources and Geotechnology* 34, No. 6, 503–525, doi:

621   10.1080/1064119X.2015.1033070.

622   Barton, Y.O., 1984. Response of pile groups to lateral loading in the centrifuge. In: Proceedings

623   of Symposium on Appl. of Centrifuge Modelling to Geotech. Design, Balkema, Rotterdam, The

624   Netherlands.

625   Bathe, K. (2006). *Finite element procedures*. Prentice Hall.

626   Beuckelaers, W. J. A. P. (2017). *Numerical Modelling of Laterally Loaded Piles for Offshore*

627   *Wind Turbines*. Ph.D. thesis, University of Oxford.

628   Bhattacharya, S. (2014). Challenges in Design of Foundations for Offshore Wind Turbines.

629   *Engineering & Technology Reference* doi: 10.1049/etr.2014.0041.

630   Boulanger, R. W., Curras, C. J., Kutter, B. L., Wilson, D. W. & Abghari, A. (1999). Seismic soil-

631   pile-structure interaction experiments and analyses. *Journal of Geotechnical and*

632   *Geoenvironmental Engineering* doi:10.1061/(ASCE)1090-0241(1999)125:9(750).

633   Boulanger, R. W., Kutter, B. L., Brandenberg, S. J., Singh, P., and Chang, D. (2003). Pile

634   foundations in liquefied and laterally spreading ground during earthquakes: Centrifuge

635   experiments and analyses. *Rep. No. Univ. of California Davis (UCD)/Center for Geotechnical*

636   *Modelling (CGM)-03/01*, Dept. of Civil Engineering, Univ. of California, Davis, CA.

637   Boussinesq, J. (1885). *Applications des potentiels a l'etude de equilibre et du mouvement des*

638   *solides elastiques*, vol. 4. GauthierVillars.

639   Broms, B.B., 1964a. Lateral resistance of piles in cohesive soils. J. Soil Mech. Found. Div. 90,

640   27–63.

641   Broms, B.B., 1964b. Lateral resistance of piles in cohesionless soils. J. Soil Mech. Found. Div.

642   90, 123–156.

643   Byrne, B. W., McAdam, R. A., Burd, H. J., Houlsby, G. T., Martin C. M., Beuckelaers, W. J. A.

644   P., Zdravkovic, L., Taborda, D. M. G., Potts, D. M., Jardine, R. J., Ushev, E., Liu, T., Abadias,

645   D., Gavin, K., Igoe, D., Doherty, P., Gretlund, J. S., Andrade, M. P., Wood, A. M., Schroeder,

646   F., Turner, S. & Plummer, M. (2017). PISA: New Design Methods for Offshore Wind Turbine

647   Monopiles. In *Offshore Site Investigation Geotechnics 8th International Conference*

648   *Proceedings,* doi:10.3723/osig17.142

649   Byrne, B. W., McAdam, R. A., Burd, H. J., Beuckelaers, W. J. A. P., Gavin, K., Houlsby, G. T.,

650   Igoe, D., Jardine, R. J., Martin, C. M., Muir Wood, A., Potts, D. M., Skov Gretlund, J.,

651   Taborda, D. M. G. & Zdravkovic, L. (2019). Monotonic laterally loaded pile testing in a stiff

652   glacial clay till at Cowden. *Geotechnique*, 1–40doi: 10.1680/jgeot.18.pisa.003.

653   Carswell, W., Arwade, S. R., DeGroot, D. J. & Myers, A. T. (2016). Natural frequency

654   degradation and permanent accumulated rotation for offshore wind turbine monopiles in clay.

655   *Renewable Energy* doi: 10.1016/j.renene.2016.05.080.

656   Chin, J.T. and Poulos, H.G., 1991. A "TZ" approach for cyclic axial loading analysis of single

657   piles. Computers and Geotechnics, 12(4), pp.289-320.

658   Cui, L. & Bhattacharya, S. (2016). Soil–monopile interactions for offshore wind turbines.

659   *Proceedings of the Institution of Civil Engineers: Engineering and Computational Mechanics*

660   169, No. 4, 171–182, doi:10.1680/jencm.16.00006.

661   Damgaard, M., Ibsen, L. B., Andersen, L. V. & Andersen, J. K. (2013). Cross-wind modal

662   properties of offshore wind turbines identified by full scale testing. *Journal of Wind*

663   *Engineering and Industrial Aerodynamics* 116, 94–108, doi:10.1016/j.jweia.2013.03.003.

664   DNV/Risø (2002). *Guidelines for Design of Wind Turbines - 2nd Edition*. doi:ISBN87-550-2870-

665   5.

666   Duncan, J. M. & Chang, C. (1970). Nonlinear analysis of stress and strain in soils. *Journal of*

667   *Soil Mechanics & Foundations Division* 96, 1629-1653

668   Gazetas, G. & Dobry, R. (1984). Simple radiation damping model for piles and footings. *Journal*

669   *of Engineering Mechanics* 110, No. 6, 937–956, doi:10.1061/(ASCE)0733-

670   9399(1984)110:6(937).

671   HM Treasury (2016). *National Infrastructure and Construction Pipeline*. See:

672   https://www.gov.uk/government/publications/national-infrastructure-and-construction-pipeline-

673   2016 Accessed 06/12/2021

674   Houlsby, G. T., Cassidy, M. J. & Einav, I. (2005). A generalised Winkler model for the behaviour

675   of shallow foundations. *Geotechnique* 55, No. 6, 449–460, doi:10.1680/geot.2005.55.6. 449.

676   Huang, A. B., Hsueh, C. K., O'Neill, M. W., Chern, S. & Chen, C. (2001). Effects of construction

677   on laterally loaded pile groups. *Journal of Geotechnical and Geoenvironmental Engineering*

678   doi: 10.1061/(ASCE)1090-0241(2001)127:5(385).

679   Klinkvort, R. T. (2012). *Centrifuge modelling of drained lateral pile - soil response: Application for*

680   *offshore wind turbine support structures*. Ph.D. thesis, Technical University of Denmark.

681   LeBlanc, C., Houlsby, G. T. & Byrne, B. W. (2010). Response of stiff piles in sand to long-term

682   cyclic lateral loading. *Geotechnique* doi: 10.1680/geot.7.00196.

683   Lombardi, D., Bhattacharya, S. & Muir Wood, D. (2013). Dynamic soil-structure interaction of

684   monopile supported wind turbines in cohesive soil. *Soil Dynamics and Earthquake*

685   *Engineering* doi: 10.1016/j.soildyn.2013.01.015.

686   Masing, G. (1926). Eigenspannumyen und verfeshungung beim messing. In *Proc. Inter.*

687   *Congress for Applied Mechanics*, pp. 332– 335.

688   Matlock, H. (1970). Correlations for design of laterally loaded piles in soft clay. In *'Proceedings*

689   *of the 2nd Annual Offshore Technology Conference (OTC)', Houston, Texas*, pp. 577 – 594.

690   Mazzoni, S., McKenna, F., Scott, M. H., Fenves, G. L. *et al.* (2006). Opensees command

691   language manual

692   McGann, C., Arduino, P., and Mackenzie-Helnwein, P. (2011). Applicability of conventional p-y

693   relations to the analysis of piles in laterally spreading soil. *J. Geotech. Geoenviron. Eng.,*

694   10.1061/(ASCE)GT .1943-5606.0000468, 557–567.

695   Musial, W., Beiter, P., Schwabe, P., Tian, T., Stehly, T. & Spitsen, P. (2016). 2016 Offshore

696   Wind Technologies Market Report.

697   Newmark, N. M. (1959). A method of computation for structural dynamics. *Journal of the*

698   *engineering mechanics division* 85, No. 3, 67–94.

699   Nikitas, G., Vimalan, N. J. & Bhattacharya, S. (2016). An innovative cyclic loading device to

700   study long term performance of offshore wind turbines. *Soil Dynamics and Earthquake*

701   *Engineering* 82, 154–160, doi:10.1016/j.soildyn.2015.12.008.

702   Page, A. M., Skau, K. S., Jostad, H. P., & Eiksund, G. R. (2017). A new foundation model for

703   integrated analyses of monopile-based offshore wind turbines. *Energy Procedia*, 137, 100-

704   107.

705 Pelecanos, L., Soga, K., Elshafie, M.Z., de Battista, N., Kechavarzi, C., Gue, C.Y., Ouyang, Y.

706   and Seo, H.J., 2018. Distributed fiber optic sensing of axially loaded bored piles. Journal of

707   Geotechnical and Geoenvironmental Engineering, 144(3), p.04017122.

708 Poulos, H.G., 1989. Cyclic axial loading analysis of piles in sand. Journal of Geotechnical

709   Engineering, 115(6), pp.836-852.

710 Prendergast, L. J. & Gavin, K. (2016). A comparison of initial stiffness formulations for small-

711   strain soil-pile dynamic Winkler modelling. *Soil Dynamics and Earthquake Engineering* 81,

712   No. November 2017, 27–41, doi:10.1016/j.soildyn.2015.11.006.

713 Prendergast, L. J., Gavin, K. & Doherty, P. (2015). An investigation into the effect of scour on

714   the natural frequency of an offshore wind turbine. *Ocean Engineering* 101, 1–11,

715   doi:10.1016/j.oceaneng. 2015.04.017.

716 Randolph, M. F. & Wroth, C. P. (1978). Analysis of deformation of vertically loaded piles.

717   *Journal of the Geotechnical Engineering Division* 104.

718 Reese LC, Welch RC. Lateral loading of deep foundations in stiff clay. J GeotechEng Div, ASCE

719   1975;101(7):633–49

720 Rosquoet, F. (2004). *Pieux Sous Charge Laterale Cyclique.* Ph.D. thesis, l'Ecole Centrale de

721   Nantes et de l'Universite de Nantes.

722 Sheil, B. B. & McCabe, B. A. (2017). Biaxial loading of offshore monopiles: Numerical modeling.

723   *International Journal of Geomechanics* 17, No. 2, 1–16, doi:10.1061/(ASCE)GM. 1943-

724   5622.0000709.

725 Shirzadeh, R., Devriendt, C., Bidakhvidi, M. A. & Guillaume, P. (2013). Experimental and

726   computational damping estimation of an offshore wind turbine on a monopile foundation.

727   *Journal of Wind Engineering and Industrial Aerodynamics* 120, 96–106, doi:

728   10.1016/j.jweia.2013.07.004.

729 Taborda, D. M. G., Zdravkovic, L., Potts, D. M., Burd, H. J., Byrne,́ B. W., Gavin, K. G.,

730   Houlsby, G. T., Jardine, R. J., Liu, T., Martin, C. M. & McAdam, R. A. (2019). Finite-element

731   modelling of laterally loaded piles in a dense marine sand at Dunkirk.

732   *Geotechnique*́, 1–16 doi:10.1680/jgeot.18.pisa.006.

733 Taciroglu, E., Rha, C. S. & Wallace, J. W. (2006). A robust macroelement model for soil-pile

734   interaction under cyclic loads.

735   *Journal of Geotechnical and Geoenvironmental Engineering* 132, No. 10, 1304–1314,

736   doi:10.1061/(ASCE)1090-0241(2006)132: 10(1304).

737 Ting, J. M. (1987). Full-scale cyclic dynamic lateral pile responses. *Journal of Geotechnical*

738   *Engineering* doi: 10.1061/(ASCE)0733-9410(1987)113:1(30).

739 Vesic, A. B. (1961). Bending of beams resting on isotropic elastic solid. *Journal of Engineering*

740   *Mechanics Division* 87.

741 Yoo, M. T., Choi, J. I., Han, J. T., and Kim, M. M. (2013). Dynamic p-y curves for dry sand by

742   dynamic centrifuge tests. *J. Earthq. Eng.,* 17(7), 1082–1102.

743 Yu, L. Q., Wang, L. Z., Guo, Z., Bhattacharya, S., Nikitas, G., Li, L. L. & Xing, Y. L. (2015).

744   Long-term dynamic behavior of monopile supported offshore wind turbines in sand.

745   doi:10.1016/j.taml.2015.02.003.

746

747

748

749

Figure captions

751

752 Figure 1. Example power spectrum of an OWT, showing rotor frequency 1P, blade passing

753 frequency 3P, and wind wave spectra (Figure adapted from Bhattacharya (2014))

754 Figure 2. Schematic diagram of a BNWF model of an OWT. The lateral soil reaction is modelled

755 with *p-y* springs and viscous dashpot dampers, and the vertical reaction with *T-z* & *q-z* springs.

756 The mass of the rotor-nacelle assembly is modelled as a point mass on the top node of the

757 OWT

758 Figure 3. A schematic of a *p-y* curve for a node experiencing gapping behaviour. This figure

759 demonstrates how the gapping parameters influence *p-y* curve

760 Figure 4. Example dynamic *p-y* curve for a cyclically loaded pile. As the value of α_p increases,

761 the pile enters the gap at increasingly larger values of *p*, and as such the gap becomes larger

762 Figure 5. Example dynamic *p-y* curves for α_y values from 0.0 to 1.0. The gapping effect
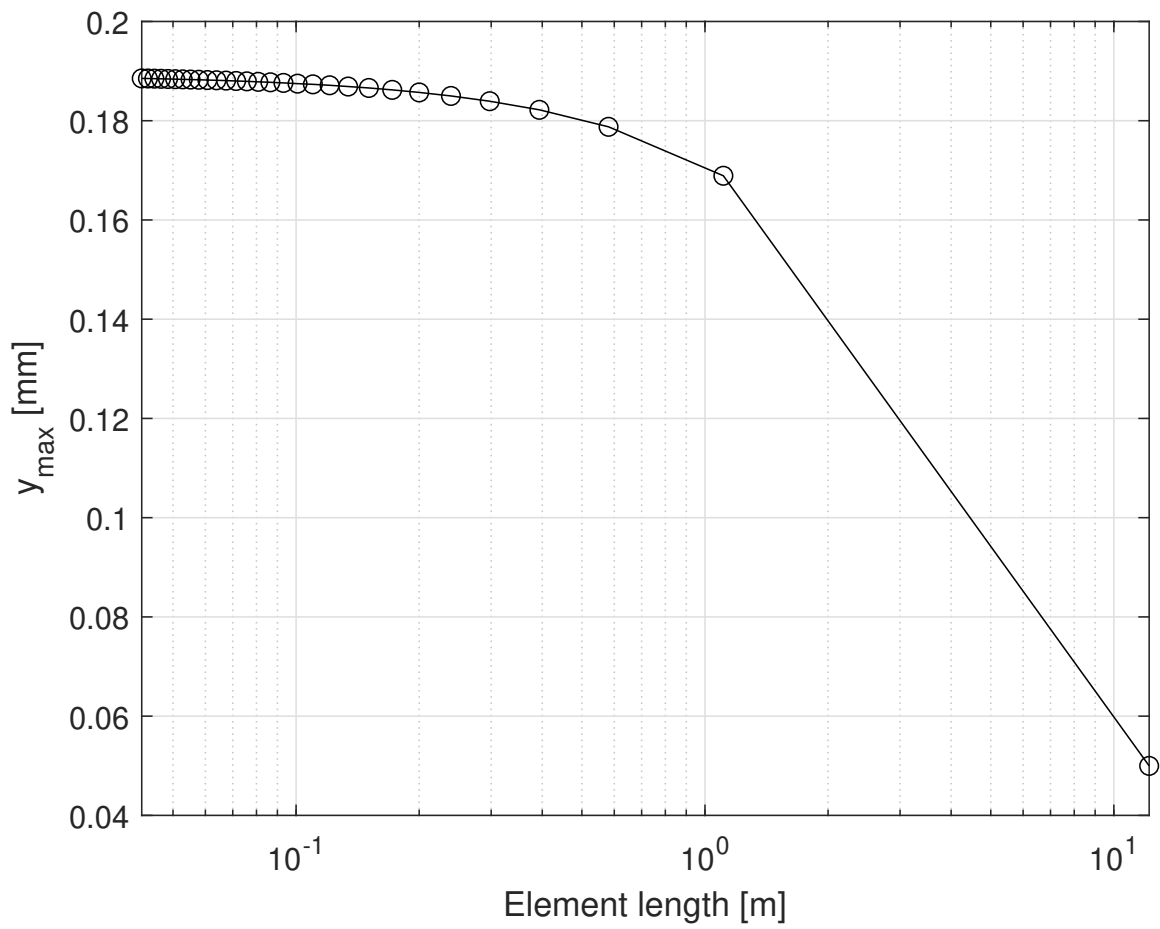
763 increases with α_y

764 Figure 6. Maximum displacement at ground level of a test pile from a dynamic push-over test for
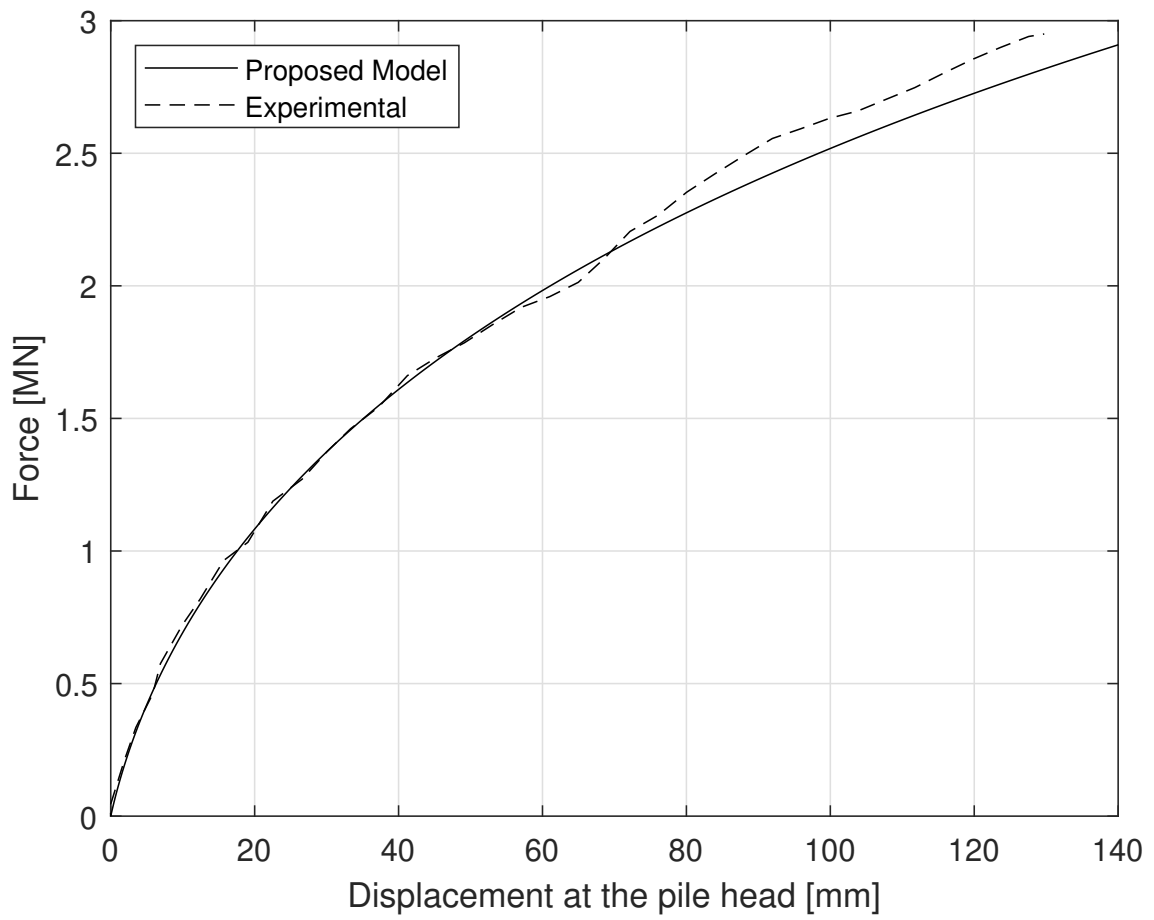
765 a changing element length

766 Figure 7. Force-displacement curve for the laterally loaded monopile test by Huang *et al.* (2001)

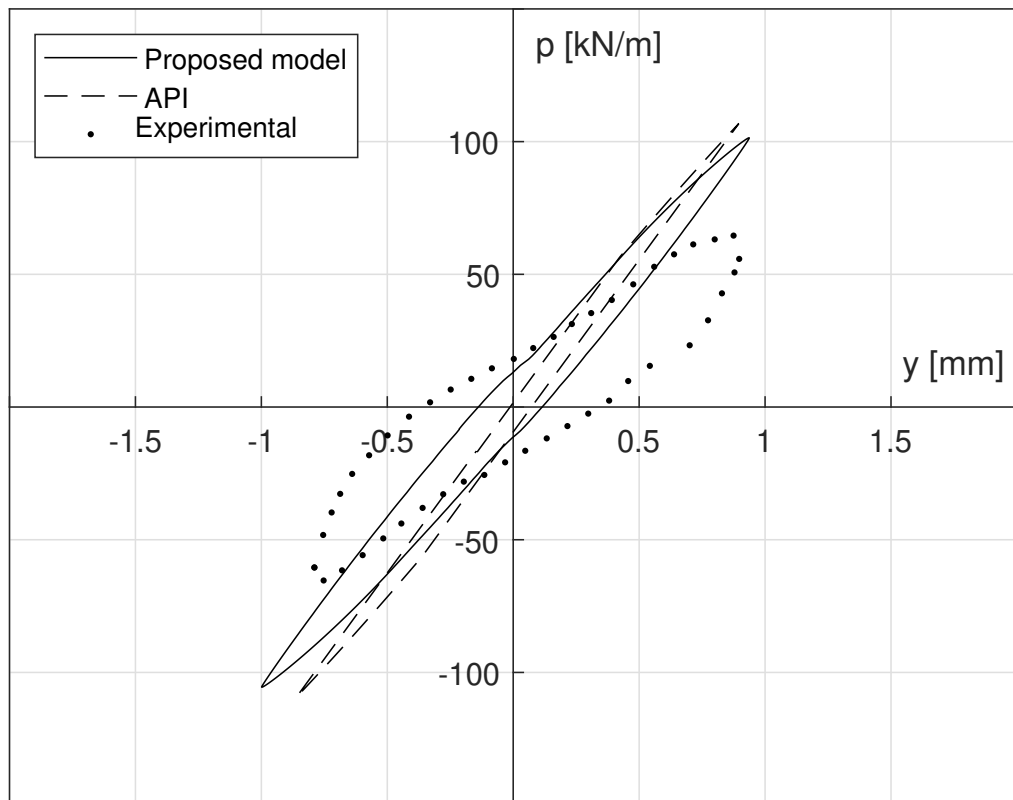767 Figure 8. Comparison of experimental, and modelled results for the static cyclic pile test (a) z =

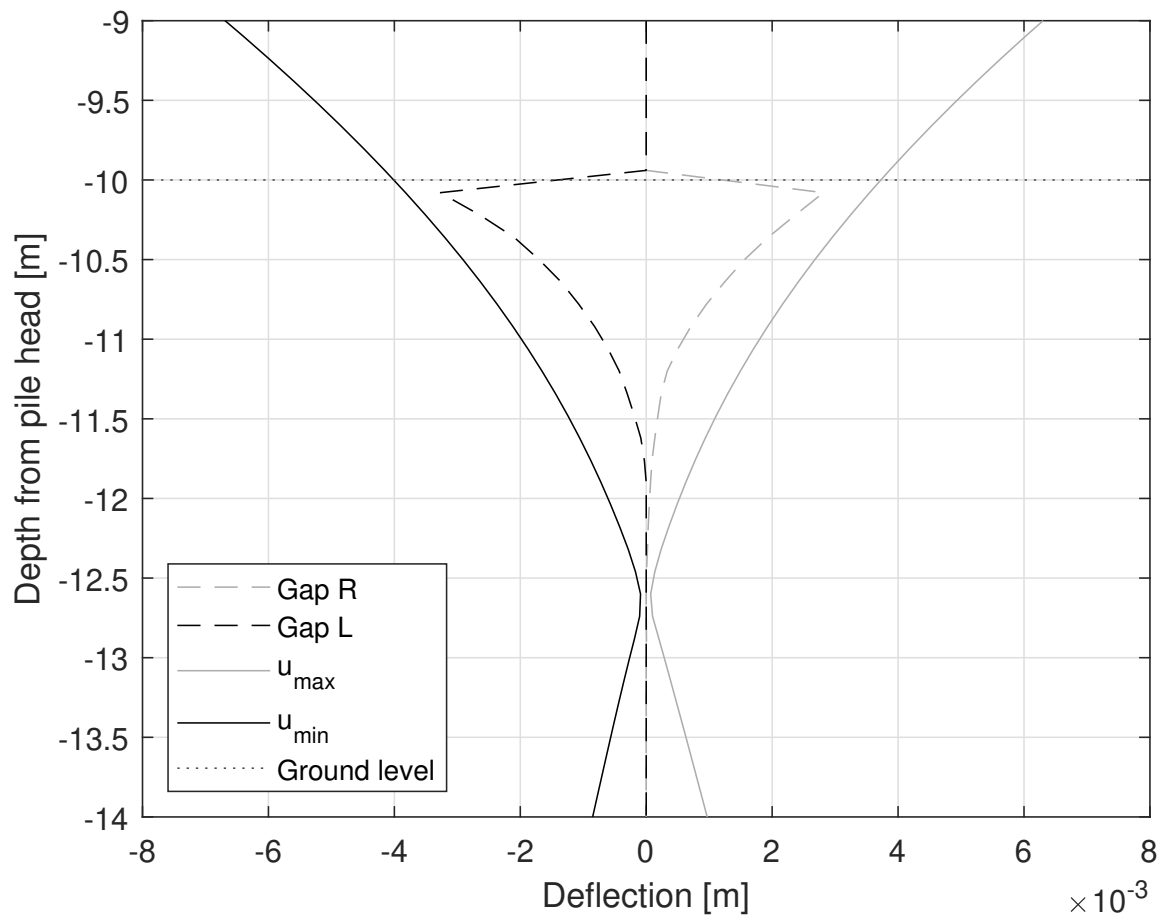768 0.5 m (b) z = 1.5 m (c) z = 3.5 m (d) Area of *p-y* loops

769 Figure 9. Profile of maximum and minimum deflection and the steady state gap size on the right
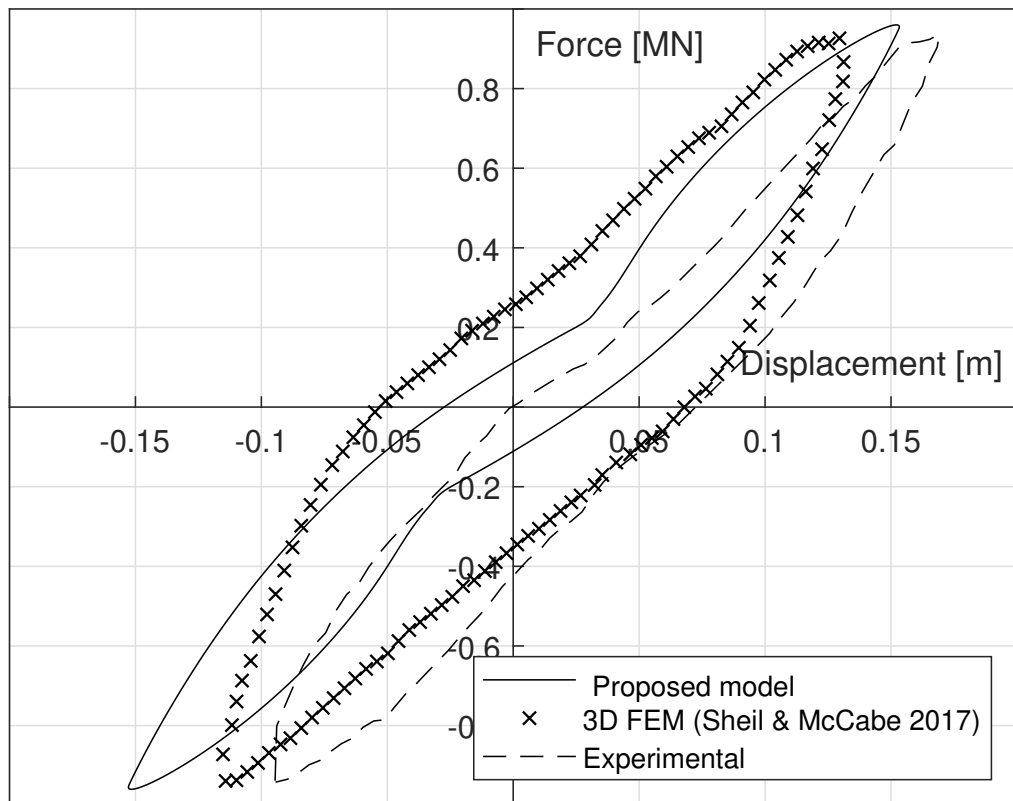
770 and left sides of the displacement profile

771 Figure 10. Static cyclic load results for test P330 performed by Rosquoet, F. (2004) (a) Force

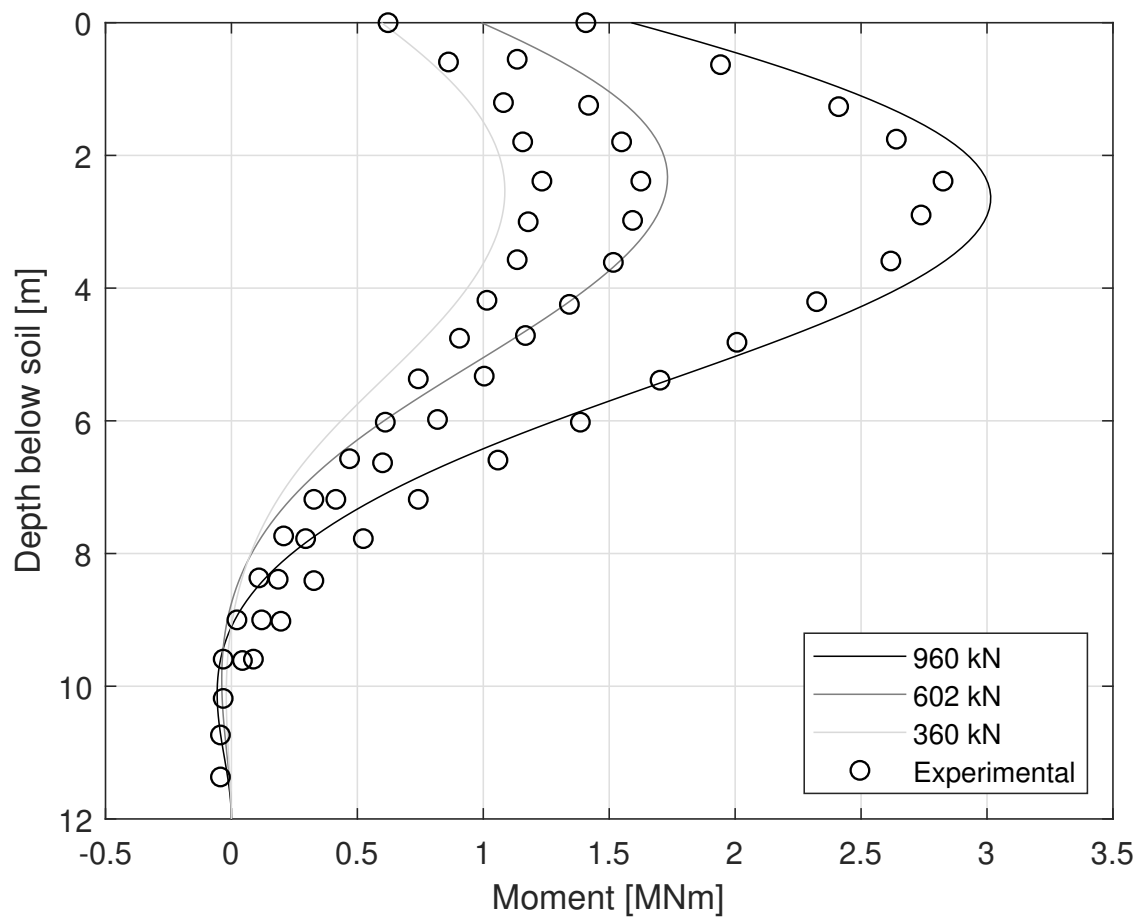772 displacement curve compared to experimental and a 3D FE model of Sheil & McCabe (2017)

773 (b) Profile of bending moment at three stages in the loading cycle, compared with experimental

774 results (c) Profile of soil reaction force at three stages in the loading cycle, compared with

775 experimental results

776 Figure 11. Profile of pile deflection with depth down the pile length (a) Proposed model results

777 (b) API results (c) Expt. Results (Ting, 1987)

778 Figure 12. Profile of moment with depth down the pile length (a) Proposed model results (b) API

779 results (c) Expt. results (Ting, 1987)

780 Figure 13. Profile of reaction force with depth down the pile length (a) Proposed model results

781 (b) API results (c) Expt. results (Ting, 1987)

782 Figure 14. Dynamic cyclic *p-y* loops of the proposed model, API curves and experimental

783 results (note scale differences) (a) Proposed model results (b) API results (c) Expt. results

784 (Ting, 1987)

785 Figure 15. Frequency spectra of the OWT model during the free vibration after a rotor stop test,

786 for the gap algorithm enabled and disabled, as well as the reference 1P frequency of the OWT.

787 The spectra peaks are located at 0.338 Hz and 0.327 Hz

788 Figure 16. Frequency response spectrum for the OWT under harmonic loading of various input

789 frequency, showing the decrease in fundamental frequency for the simulation including gapping

790   Figure 17. Profile of maximum and minimum deflection of the OWT foundation, and the steady

791   state gap formed on the right and left sides of the pile. The gap is significant to a depth of

792   approximately 85 m

793   Figure 18. Acceleration time history of the OWT model during a rotor stop simulation. The

794   output of simulations with and without the gapping algorithm are presented

795

796   Table 1. Details of the case studies examined in this report, and the gapping parameters used

797   to model them.

798
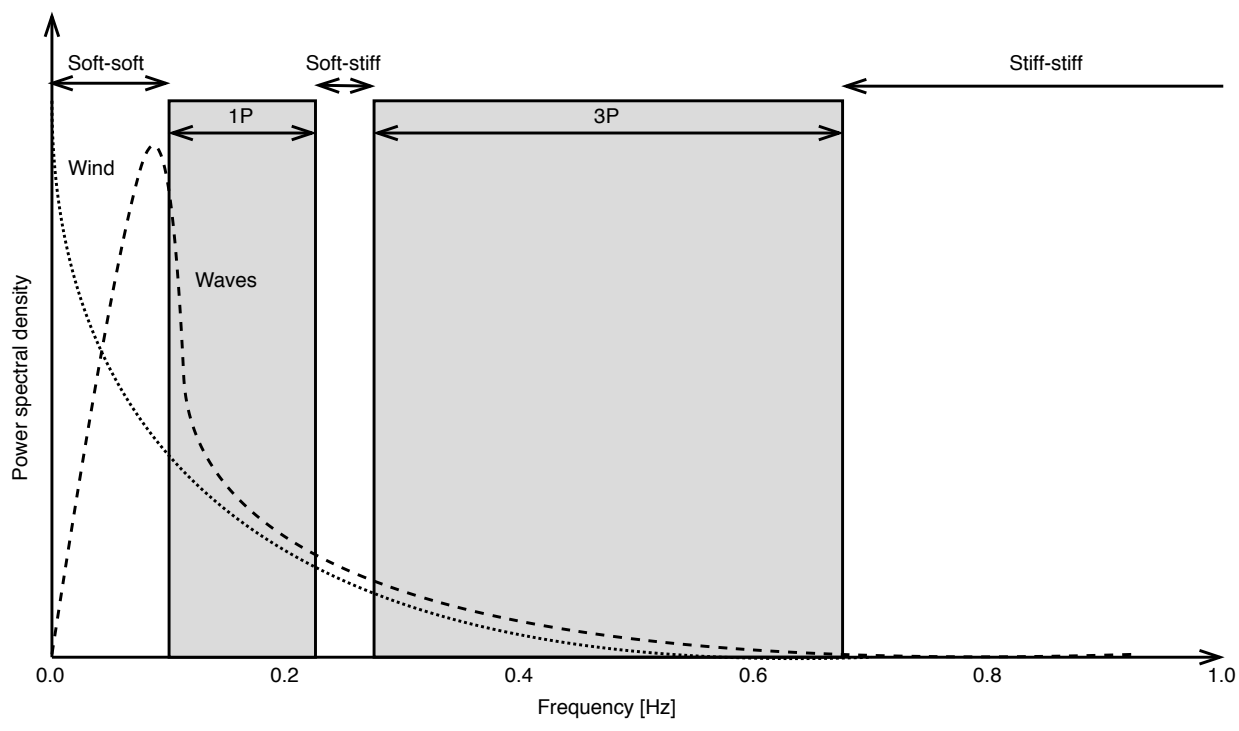
Figure 1: Example power spectrum of an OWT, showing rotor frequency 1P, blade passing frequency 3P, and wind wave spectra (Figure adapted from Bhattacharya (2014))
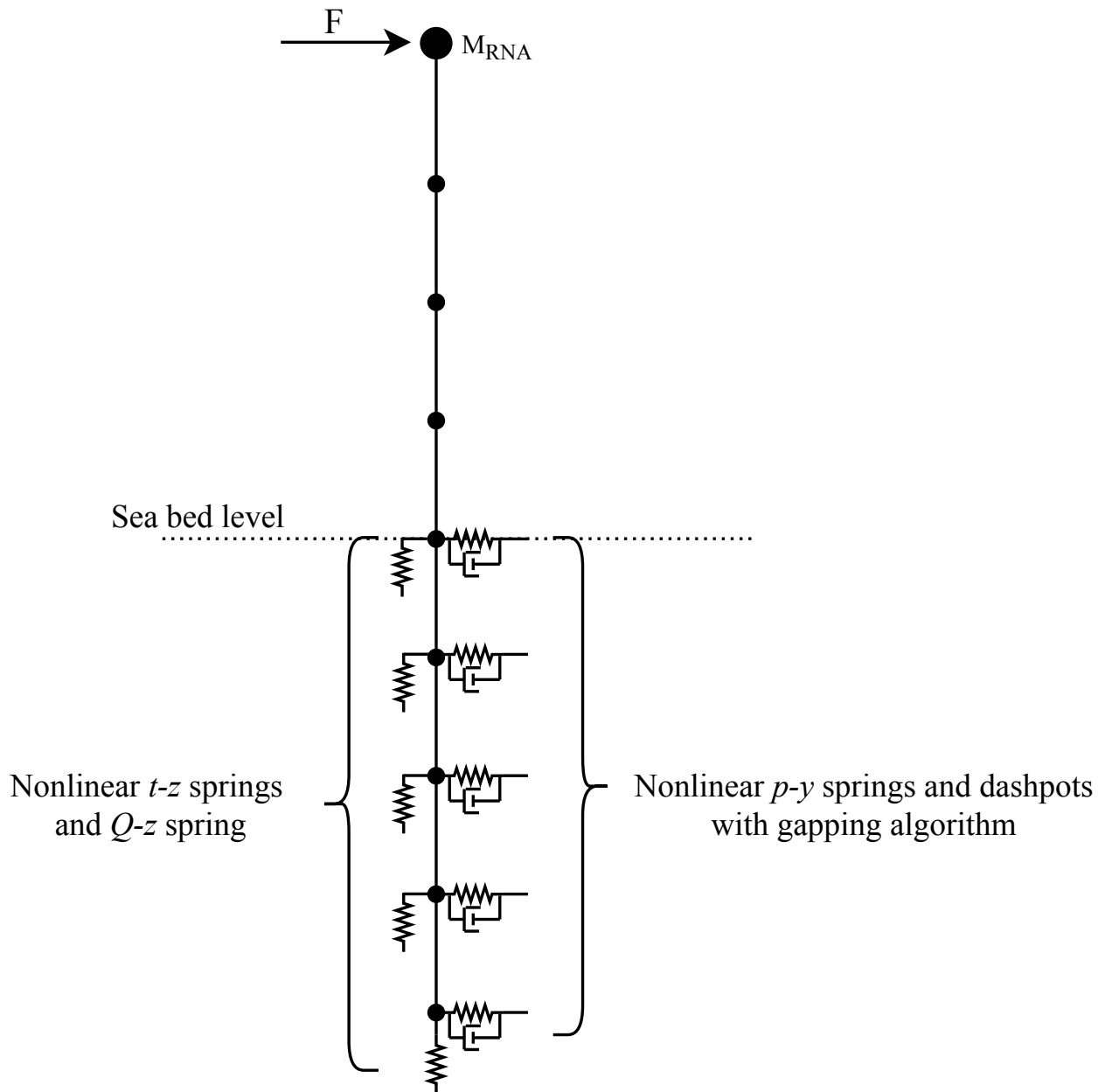
Figure 2: Schematic diagram of a BNWF model of an OWT. The lateral soil reaction is modelled with p-y springs and viscous dashpot dampers, and the vertical reaction with T-z & q-z springs. The mass of the rotor-nacelle assembly is modelled as a point mass on the top node of the OWT
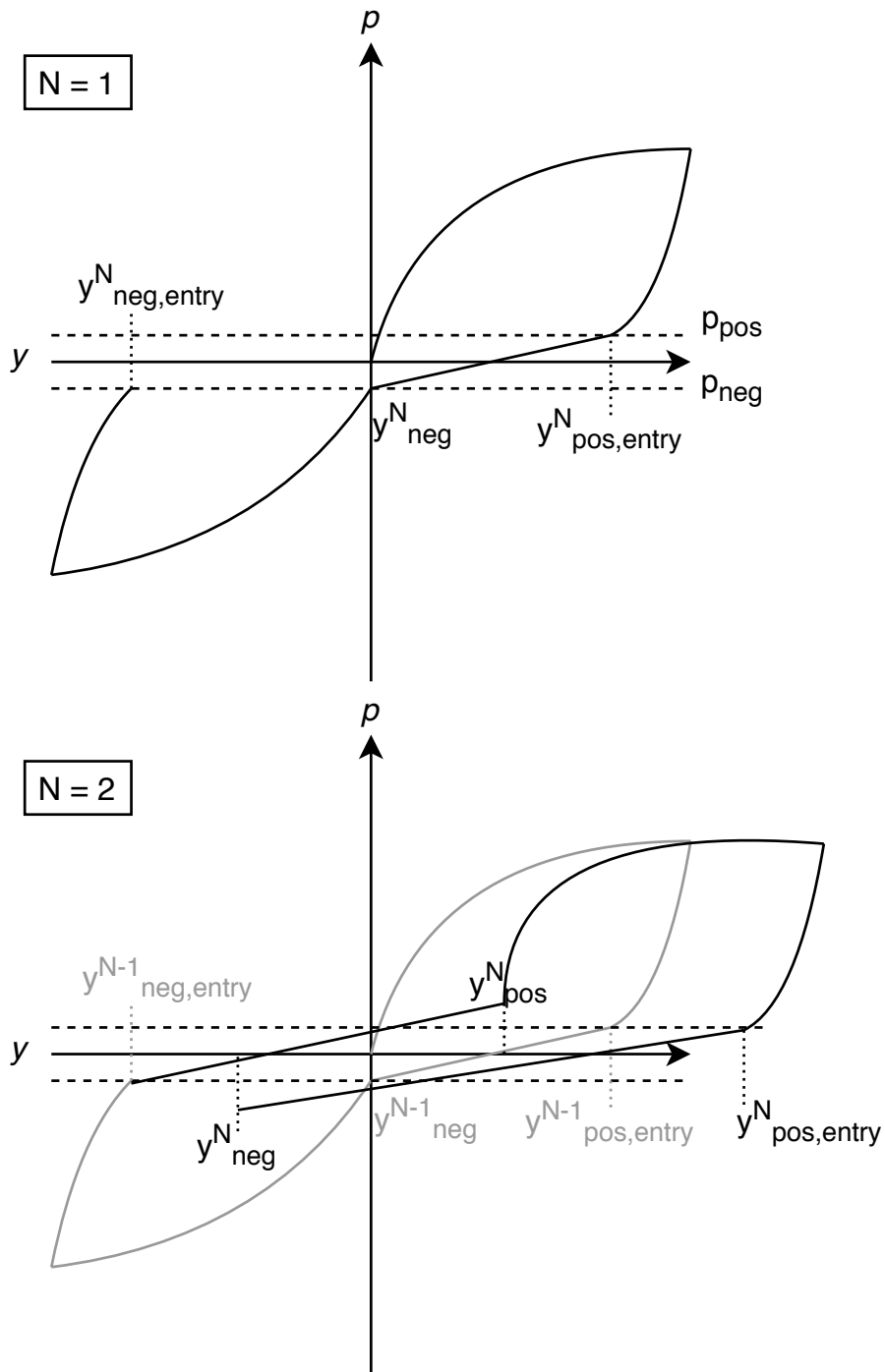
Figure 3: A schematic of a p-y curve for a node experiencing gapping behaviour. This figure demonstrates how the gapping parameters influence p-y curve
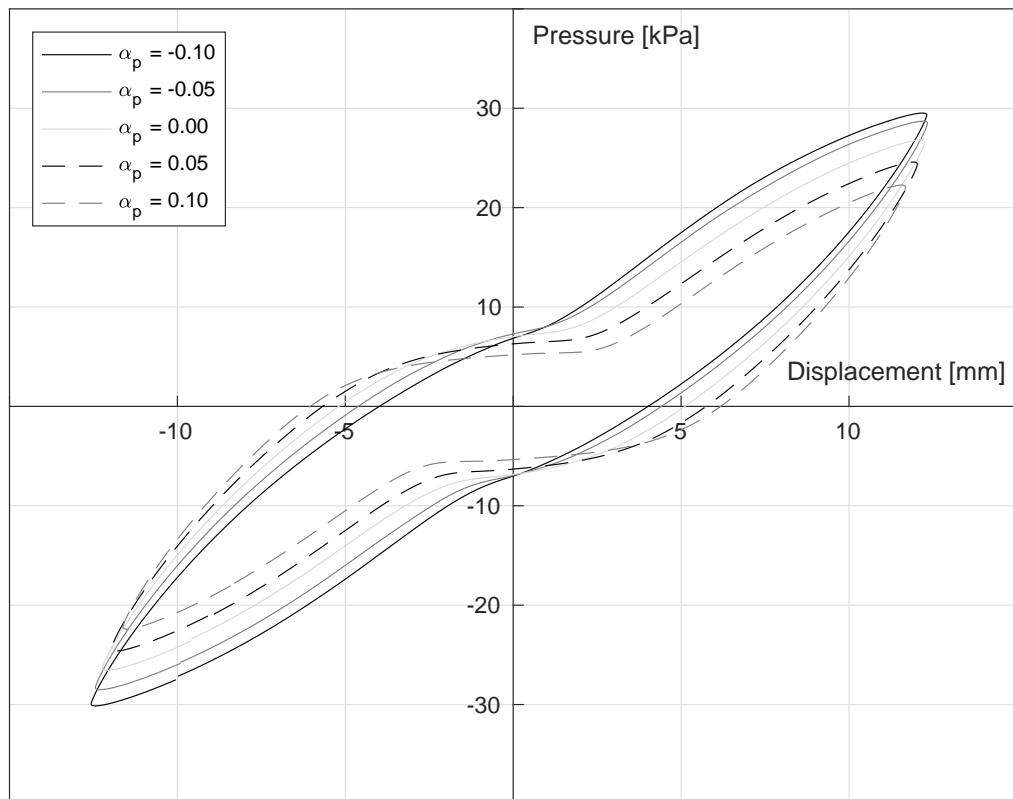
Figure 4: Example dynamic p-y curve for a cyclically loaded pile. As the value of α_p increases, the pile enters the gap at increasingly larger values of p, and as such the gap becomes larger
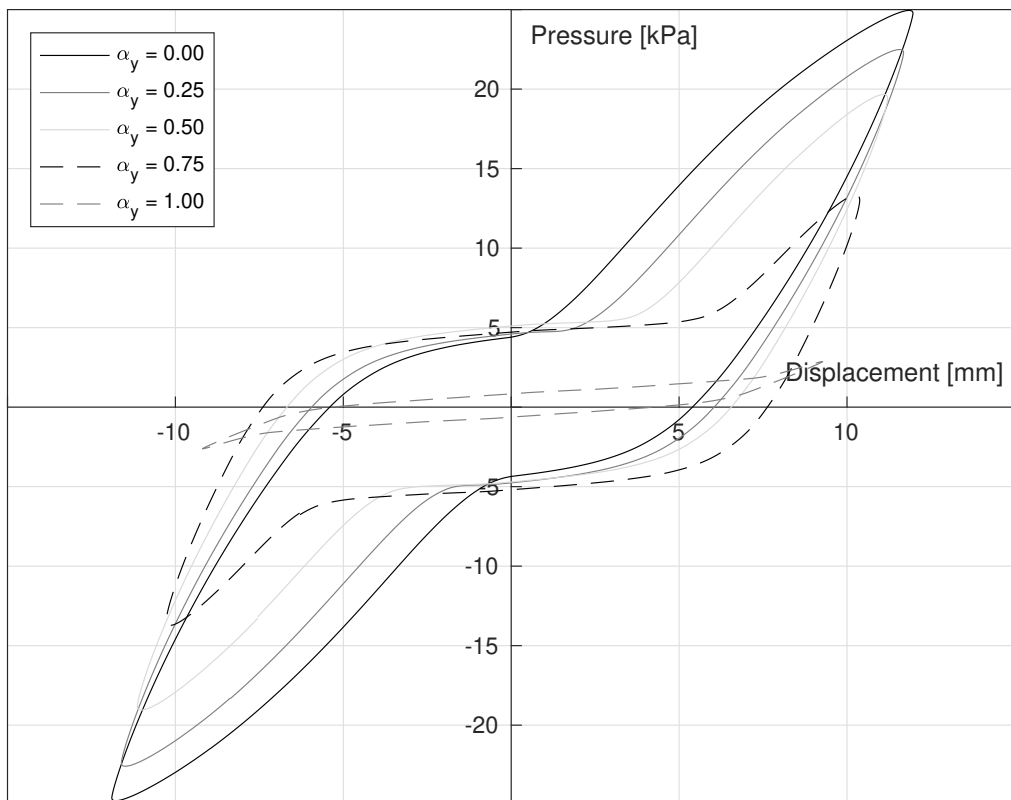
Figure 5: Example dynamic p-y curves for α_y values from 0.0 to 1.0. The gapping effect increases with α_y

Figure 6: Maximum displacement at ground level of a test pile from a dynamic push-over test for a changing element length

Figure 7: Force-displacement curve for the laterally loaded monopile test by Huang et al. (2001)
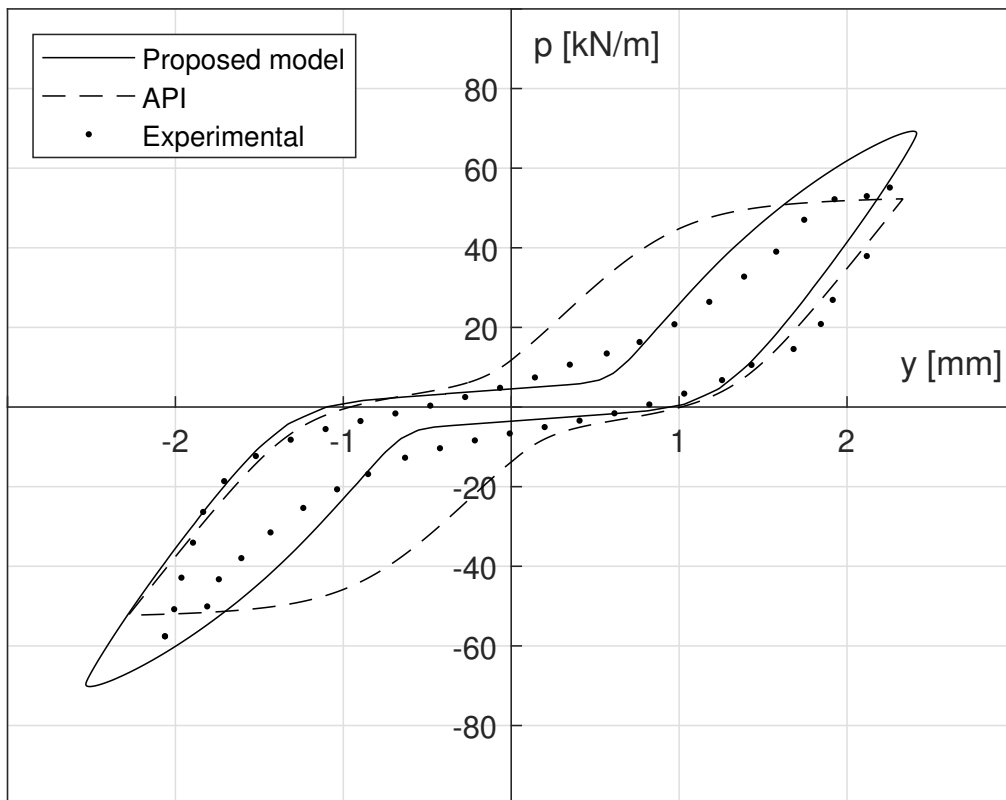
Figure 8a: Comparison of experimental, and modelled results for the static cyclic pile test (a) z = 0.5 m

Figure 8b: Comparison of experimental, and modelled results for the static cyclic pile test (b) z = 1.5 m
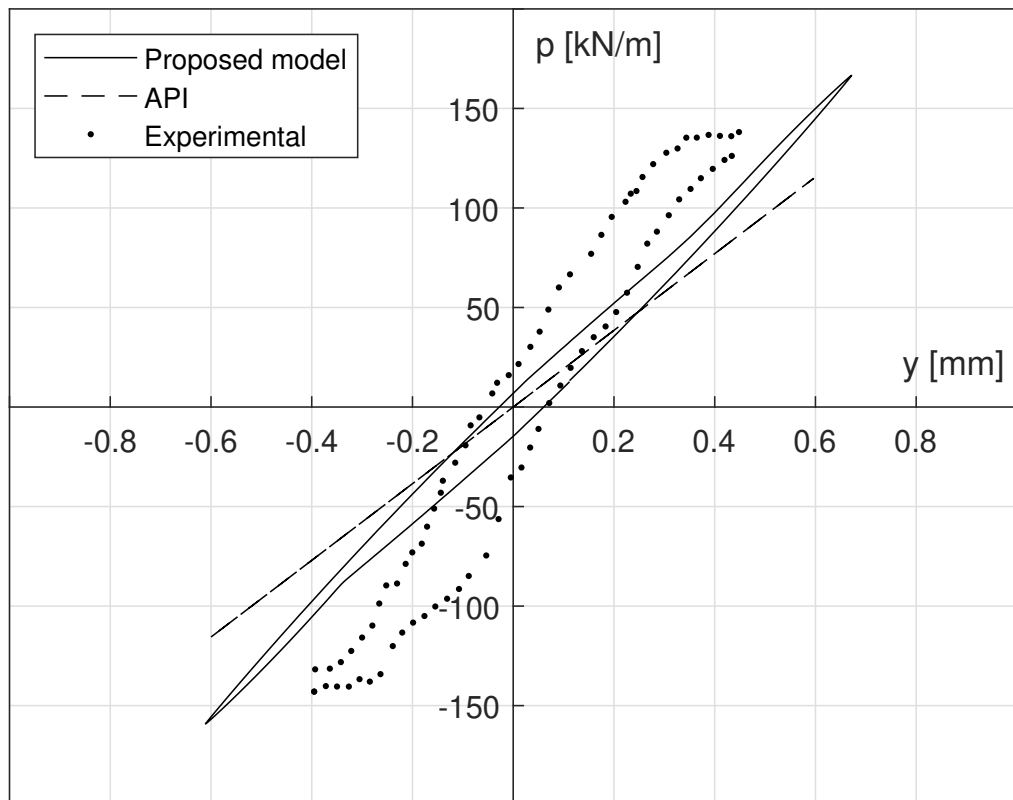
Figure 8c: Comparison of experimental, and modelled results for the static cyclic pile test (c) z = 3.5 m
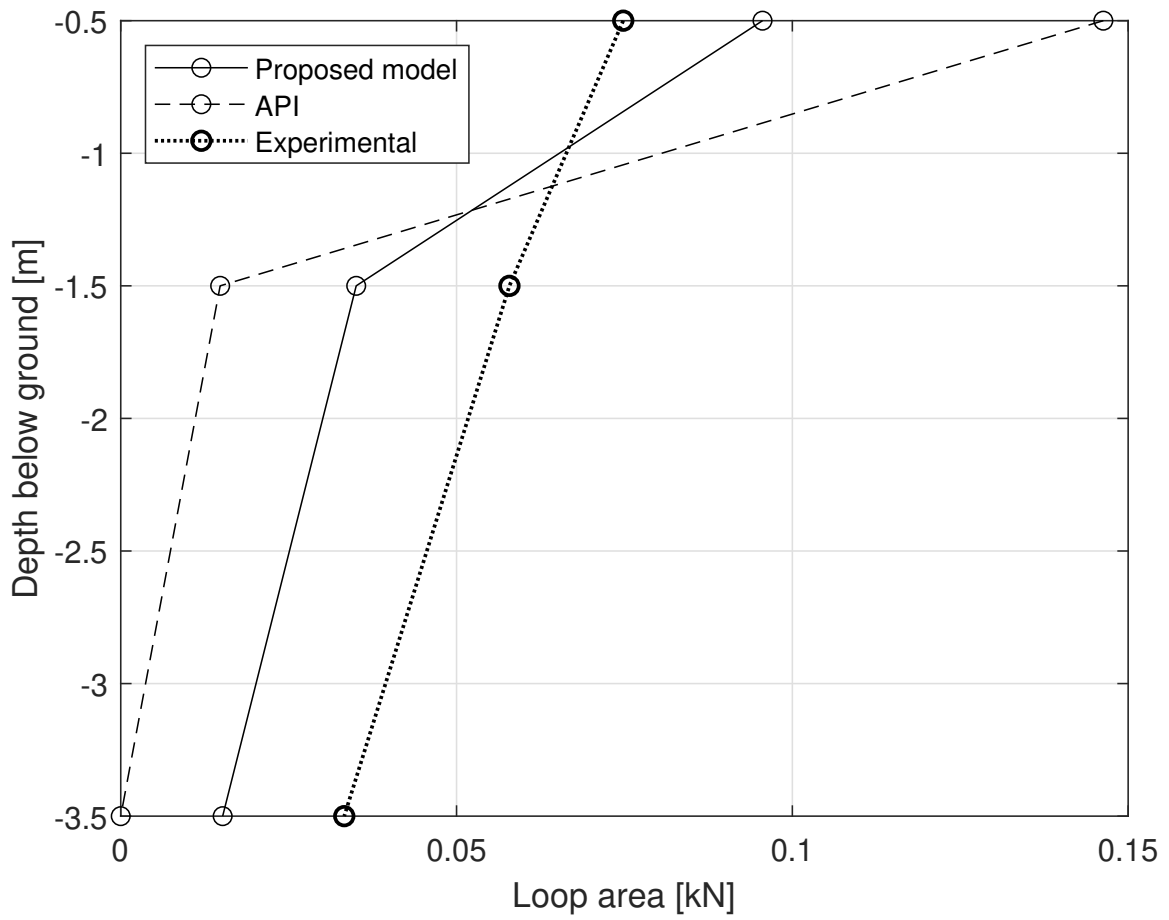
Figure 8d: Comparison of experimental, and modelled results for the static cyclic pile test (d) Area of p-y loops

Figure 9: Profile of maximum and minimum deflection and the steady state gap size on the right and left sides of the displacement profile

Figure 10a: Static cyclic load results for test P330 performed by Rosquoet (2004) (a) Force displacement curve compared to experimental and a 3D FE model of Sheil & McCabe (2017)

Figure 10b: Static cyclic load results for test P330 performed by Rosquoet (2004) (b) Profile of bending moment at three stages in the loading cycle, compared with experimental results
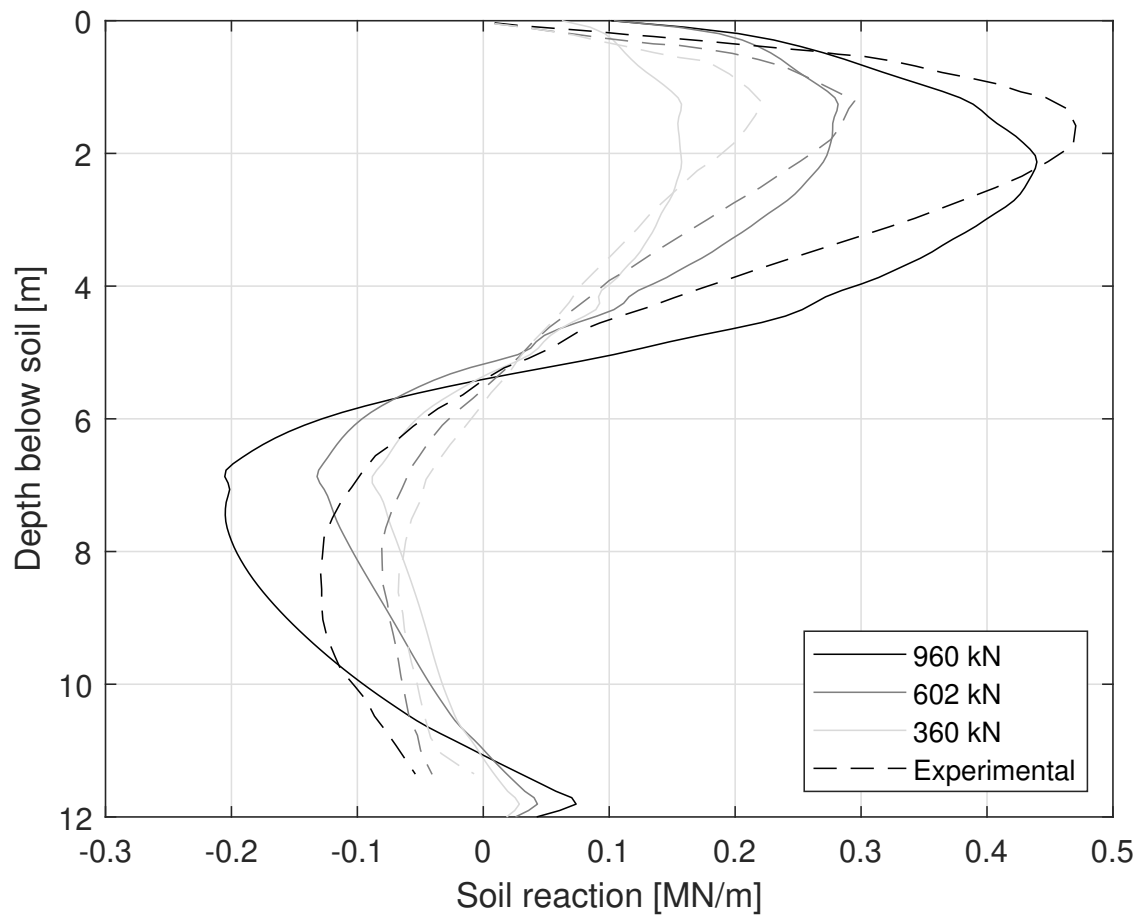
Figure 10c: Static cyclic load results for test P330 performed by Rosquoet (2004) (c) Profile of soil reaction force at three stages in the loading cycle, compared with experimental results
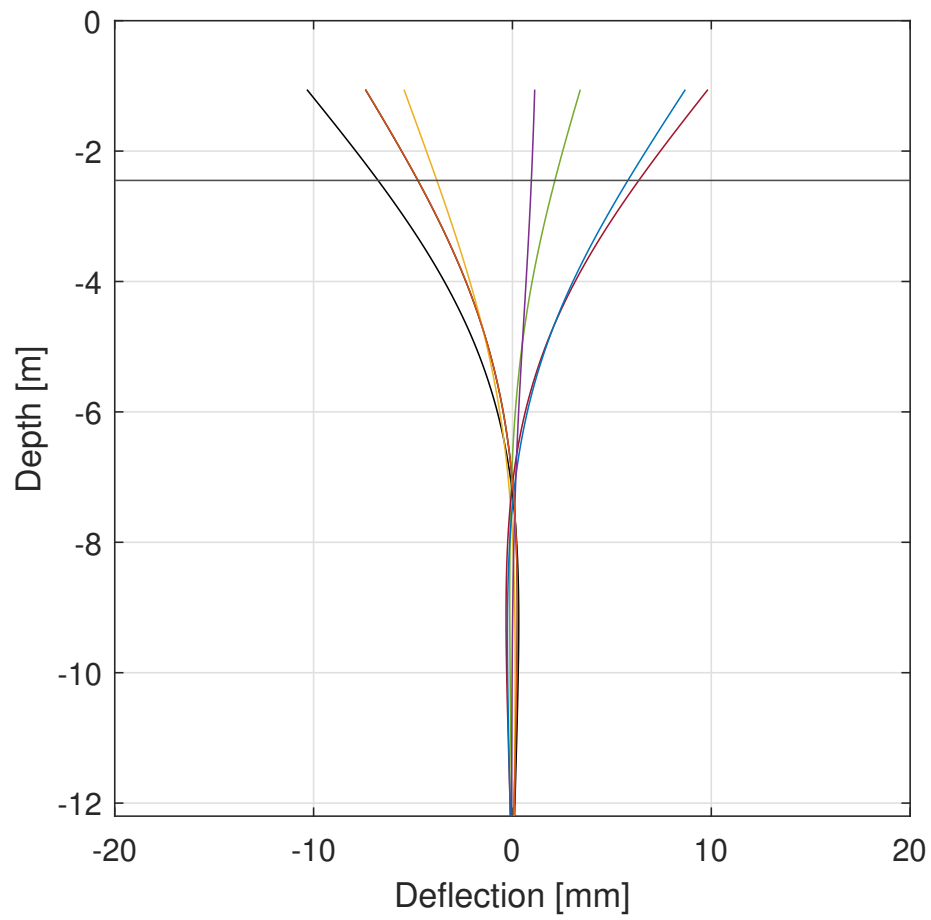
Figure 11a: Profile of pile deflection with depth down the pile length (a) Proposed model results
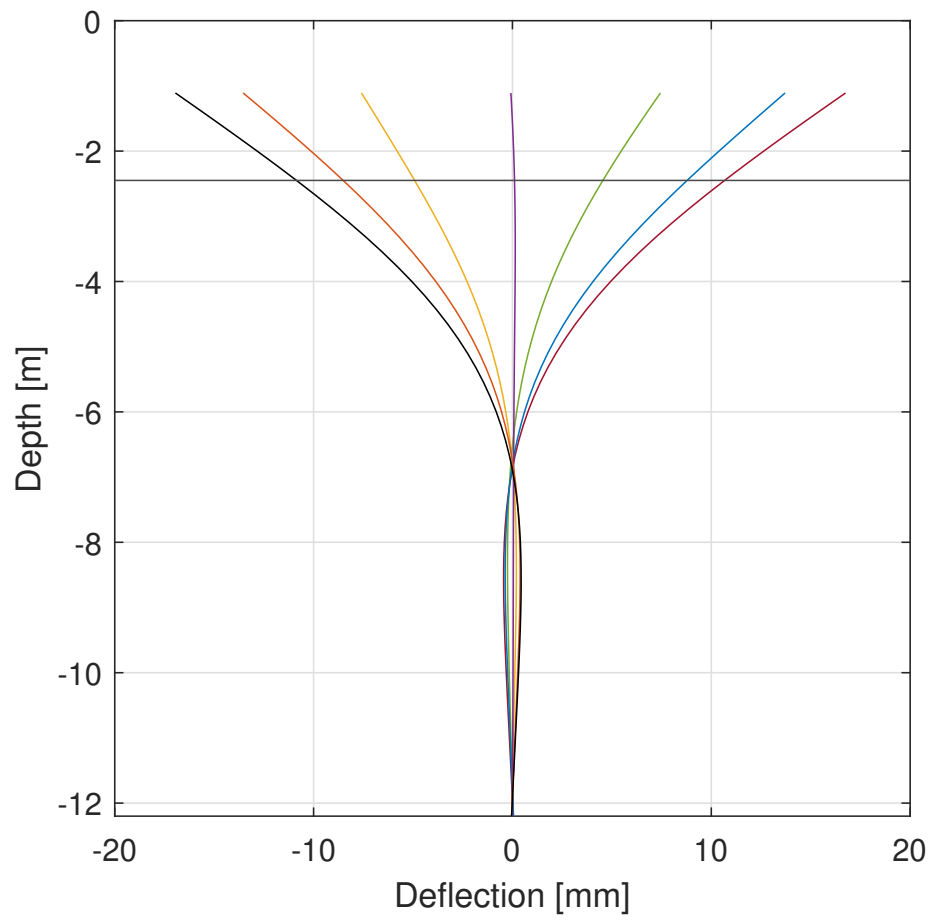
Figure 11b: Profile of pile deflection with depth down the pile length (b) API results
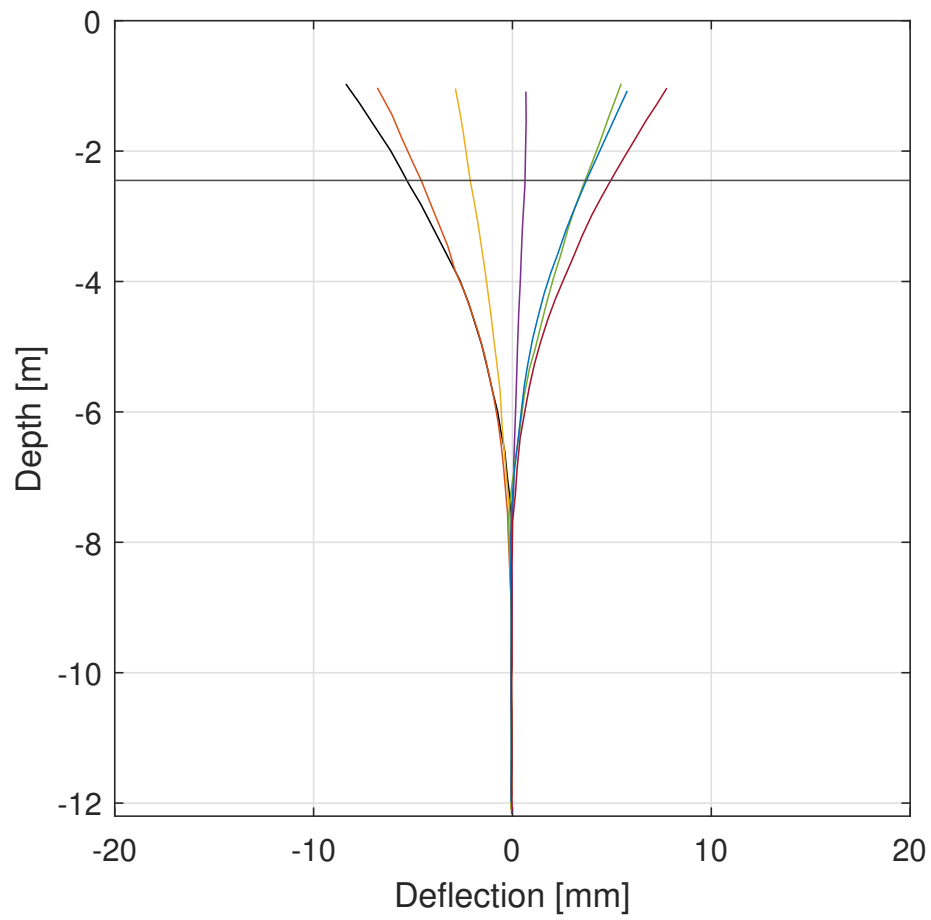
Figure 11c: Profile of pile deflection with depth down the pile length (c) Expt. Results (Ting, 1987)
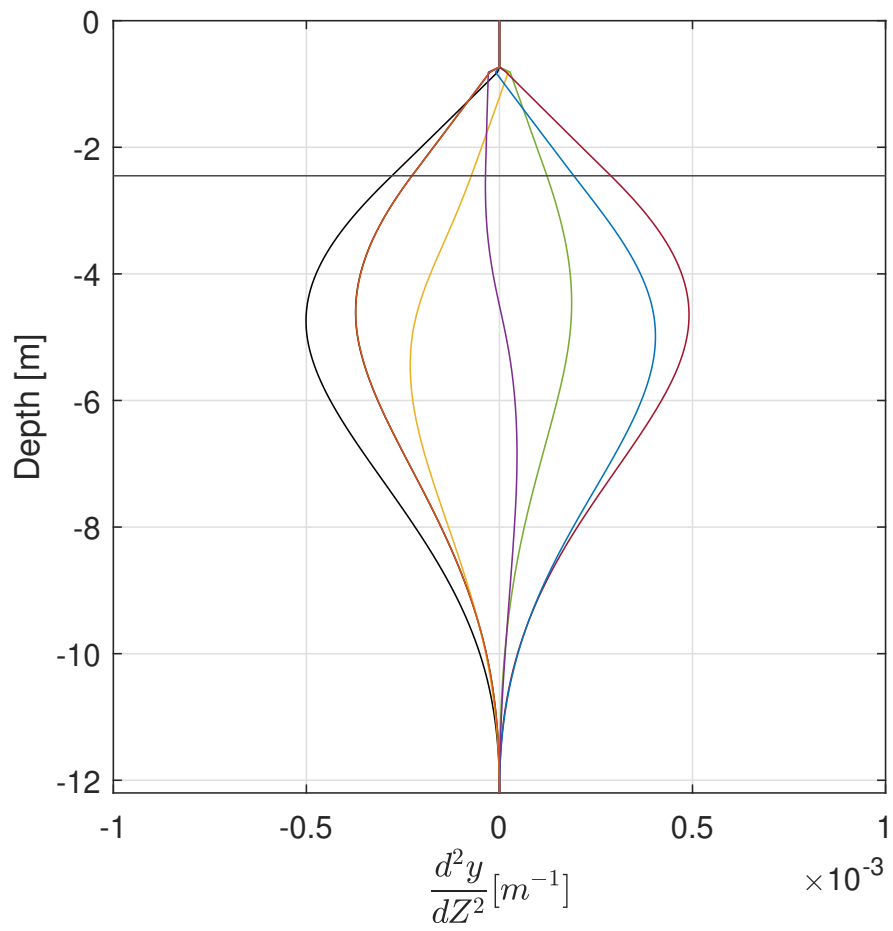
Figure 12a: Profile of moment with depth down the pile length (a) Proposed model results
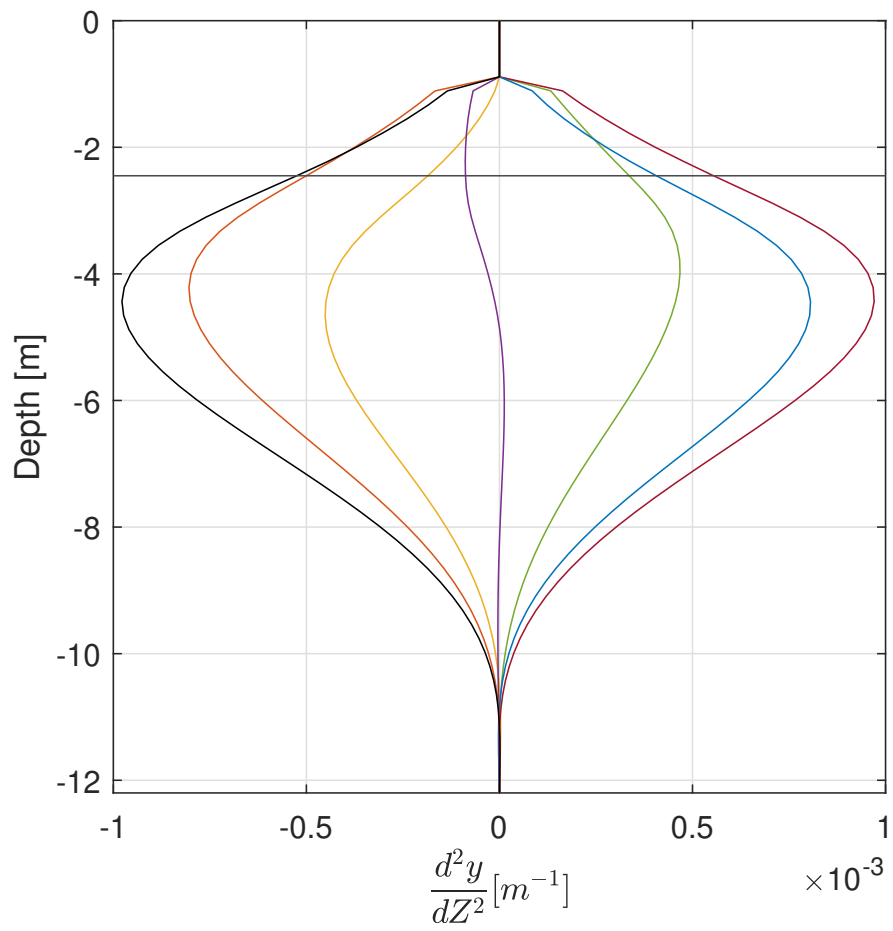
Figure 12b: Profile of moment with depth down the pile length (b) API results
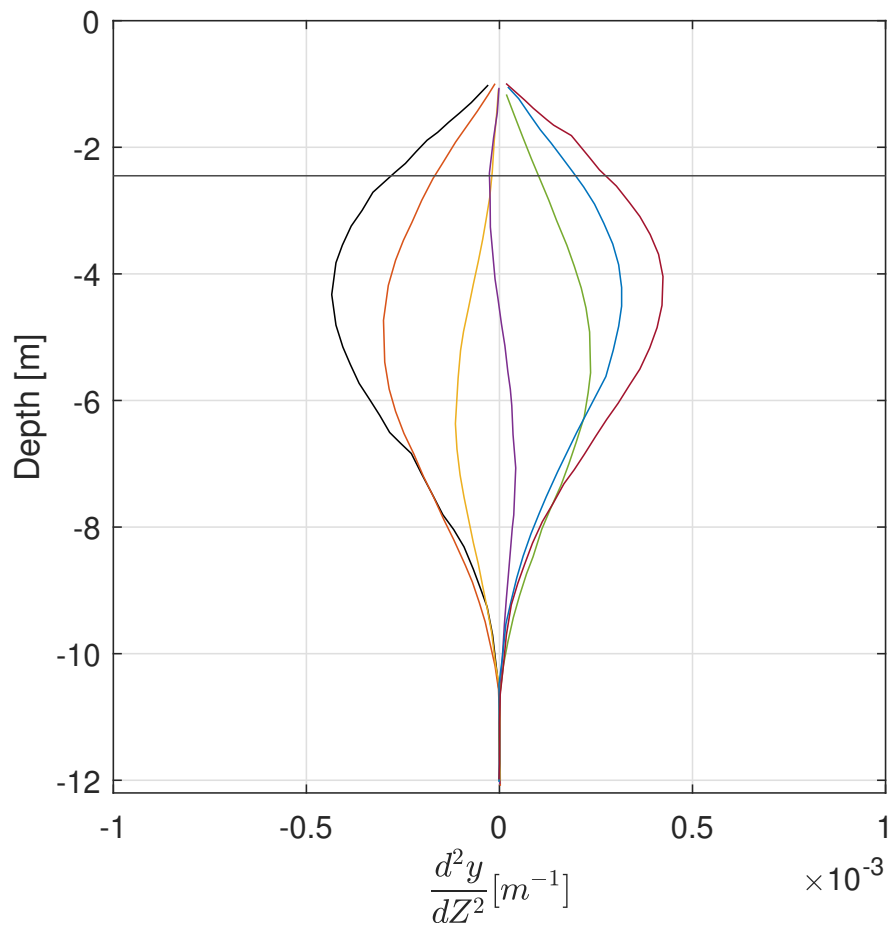
Figure 12c: Profile of moment with depth down the pile length (c) Expt. Results (Ting, 1987)
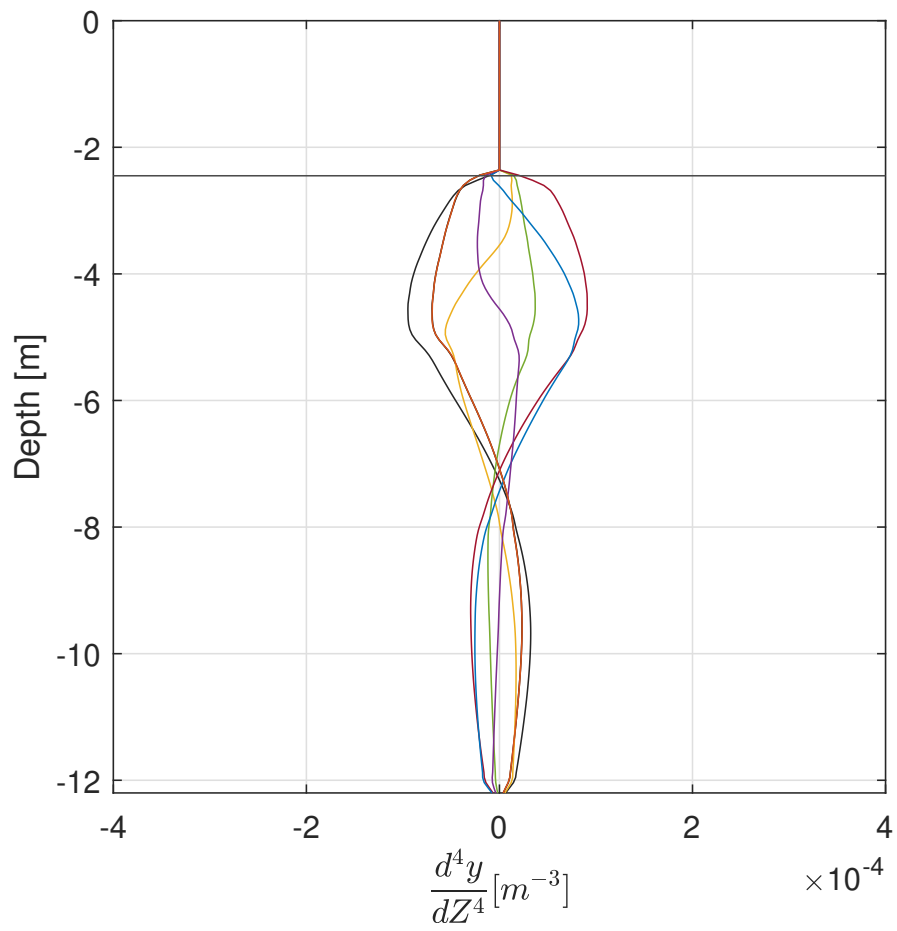
Figure 13a: Profile of reaction force with depth down the pile length (a) Proposed model results
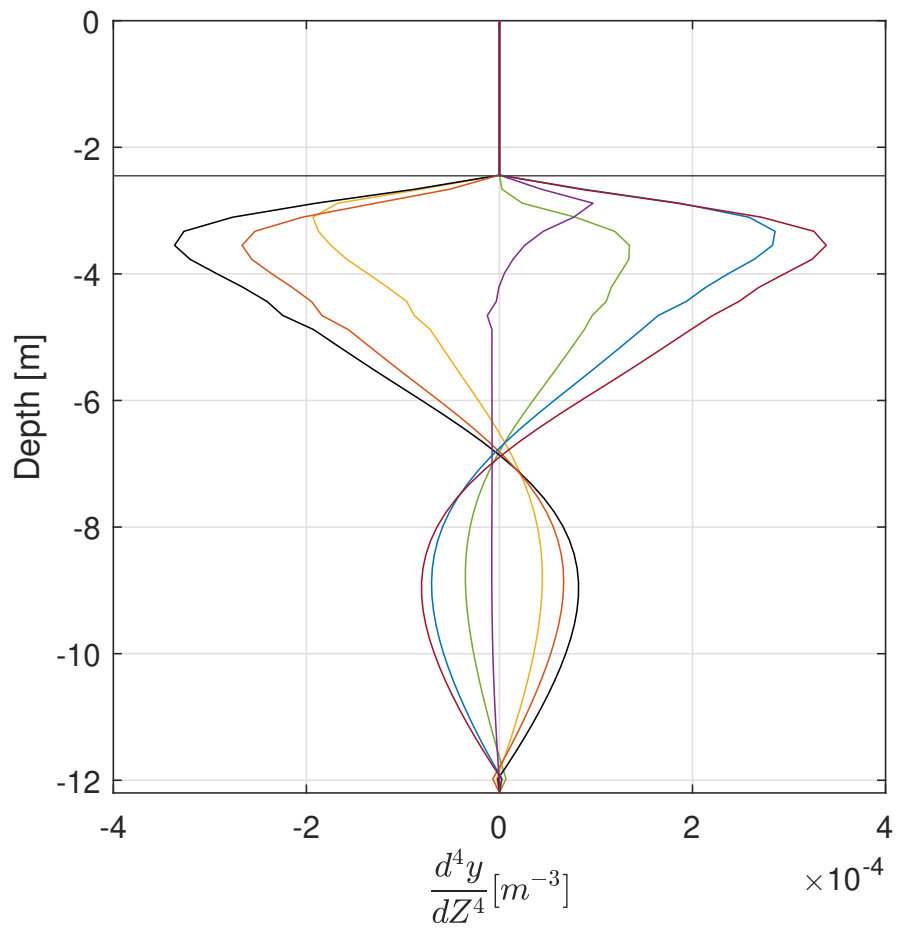
Figure 13b: Profile of reaction force with depth down the pile length (b) API results
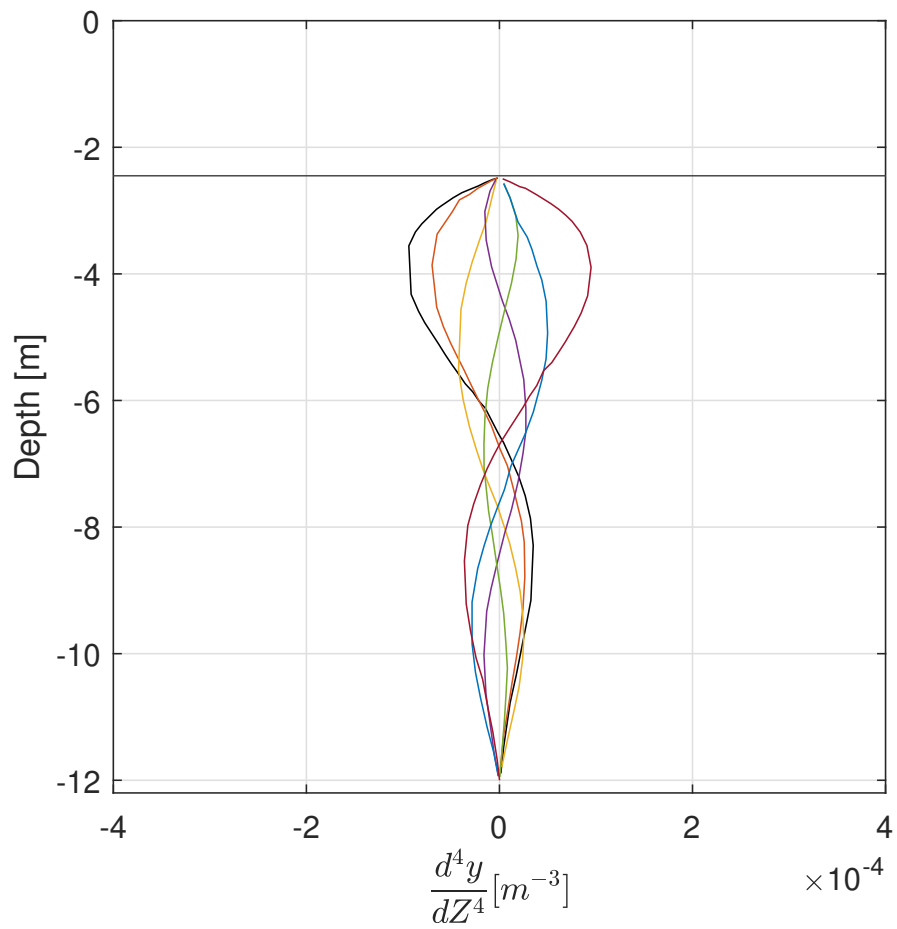
Figure 13c: Profile of reaction force with depth down the pile length (c) Expt. Results (Ting, 1987)
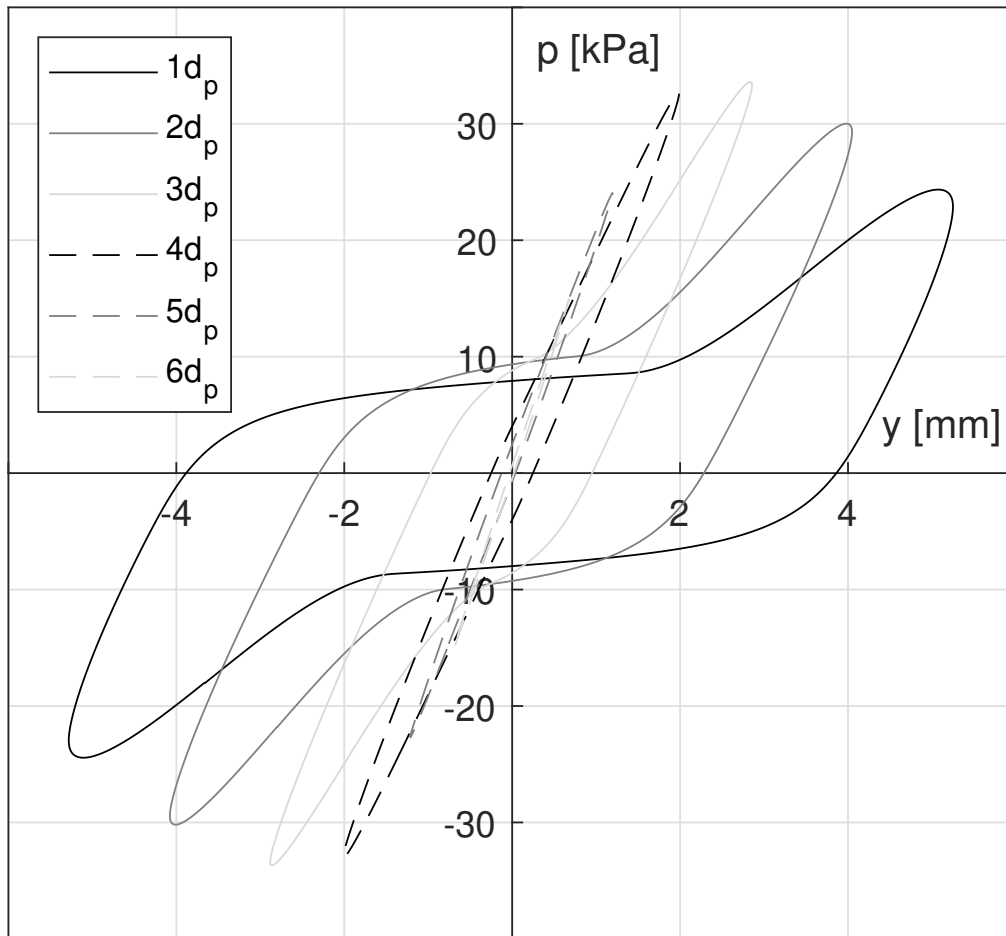
Figure 14a: Dynamic cyclic p-y loops of the proposed model, API curves and experimental results (note scale differences) (a) Proposed model results
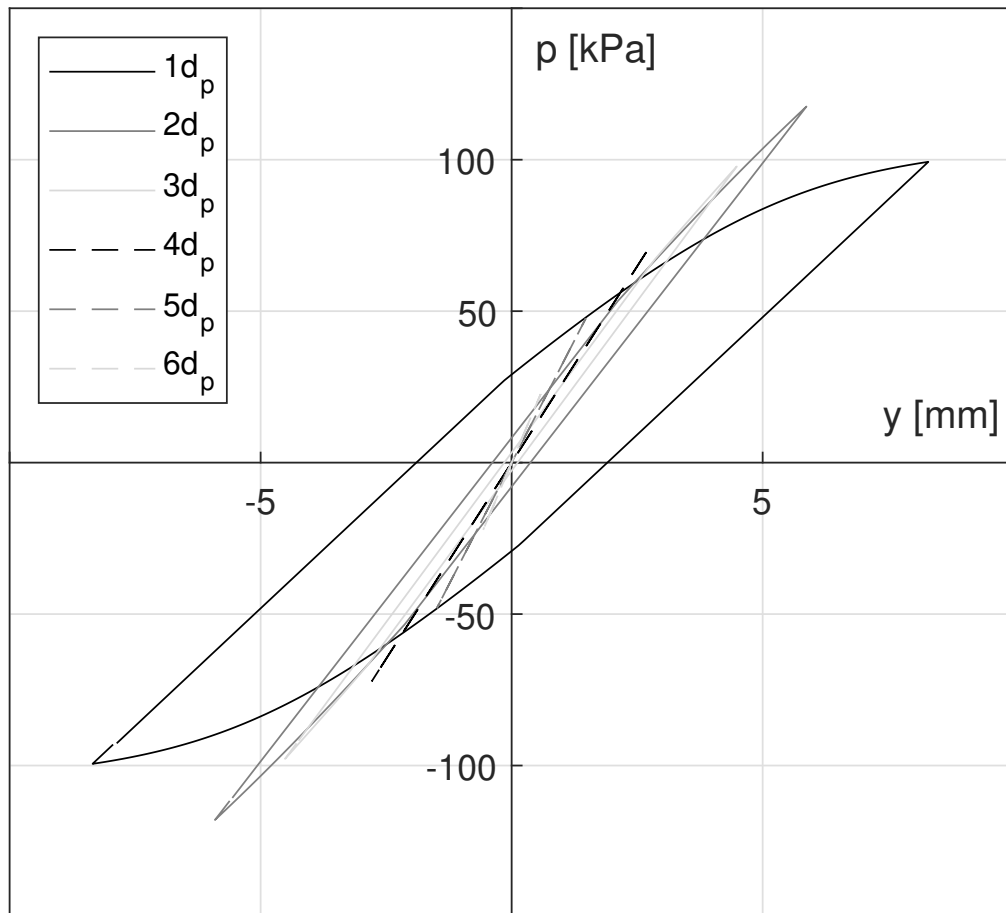
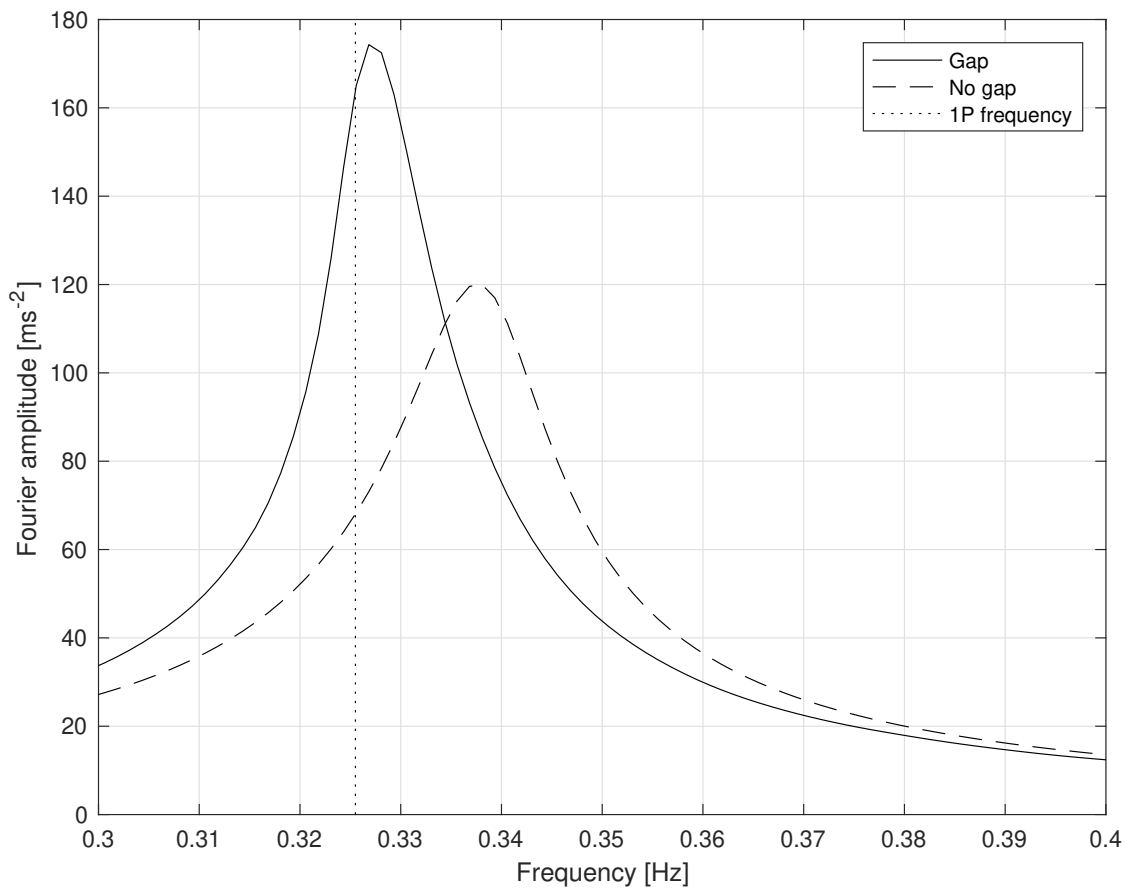Figure 14b: Dynamic cyclic p-y loops of the proposed model, API curves and experimental results (note scale differences) (b) API results
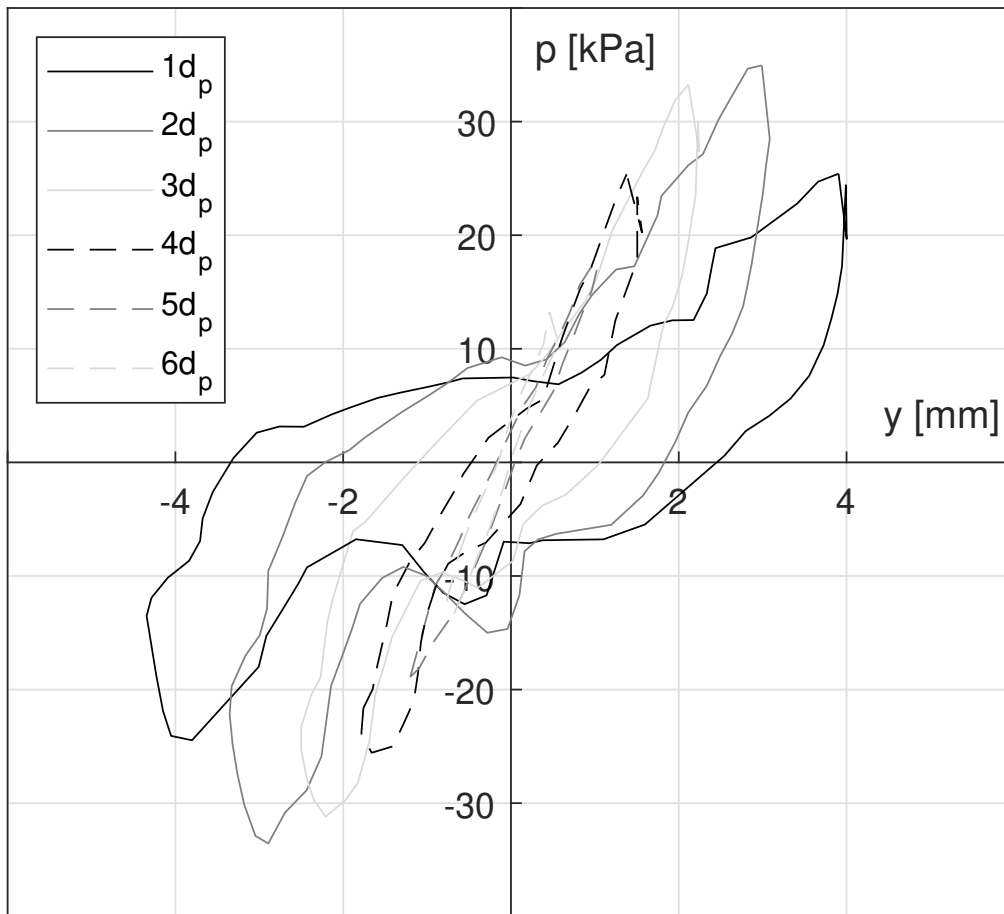
Figure 14c: Dynamic cyclic p-y loops of the proposed model, API curves and experimental results (note scale differences) (c) Expt. Results (Ting, 1987)

Figure 15: Frequency spectra of the OWT model during the free vibration after a rotor stop test, for the gap algorithm enabled and disabled, as well as the reference 1P frequency of the OWT. The spectra peaks are located at 0.338 Hz and 0.327 Hz
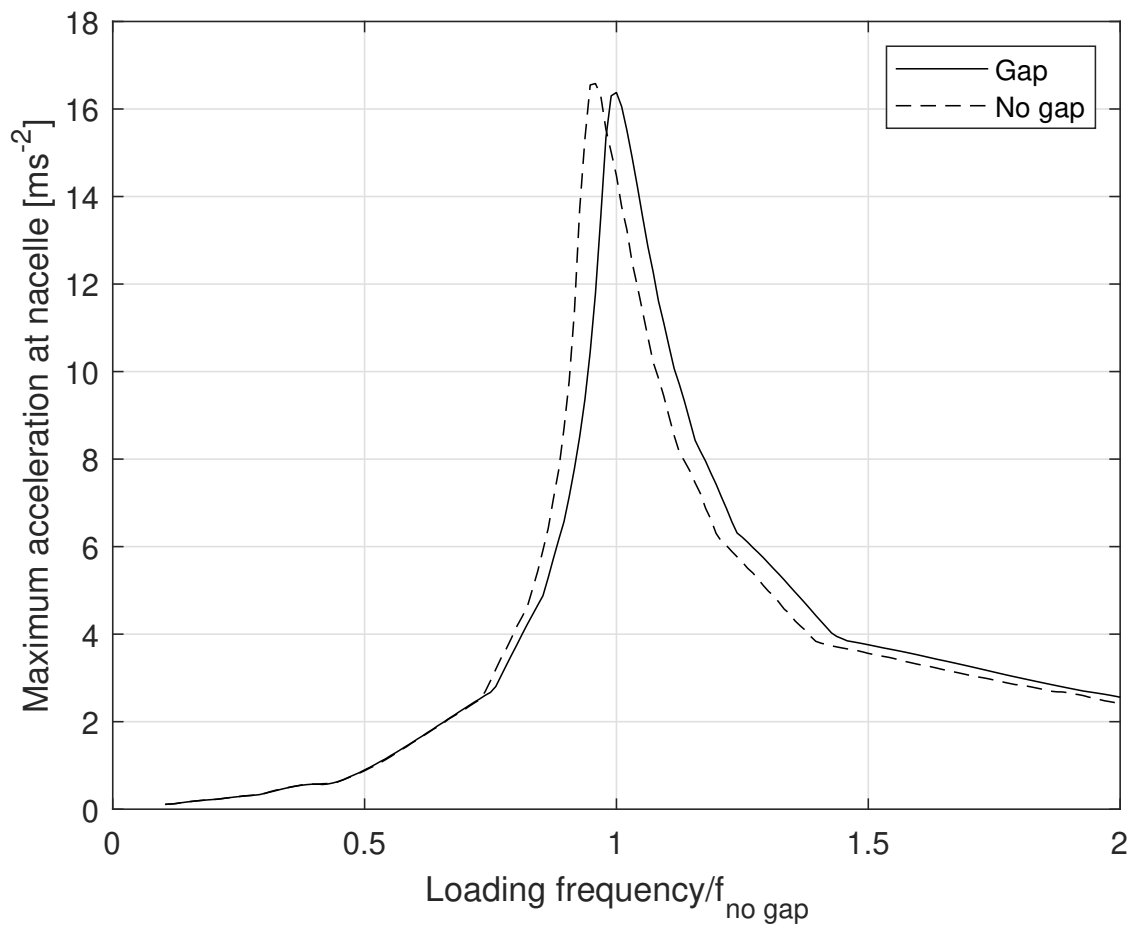
Figure 16: Frequency response spectrum for the OWT under harmonic loading of various input frequency, showing the decrease in fundamental frequency for the simulation including gapping
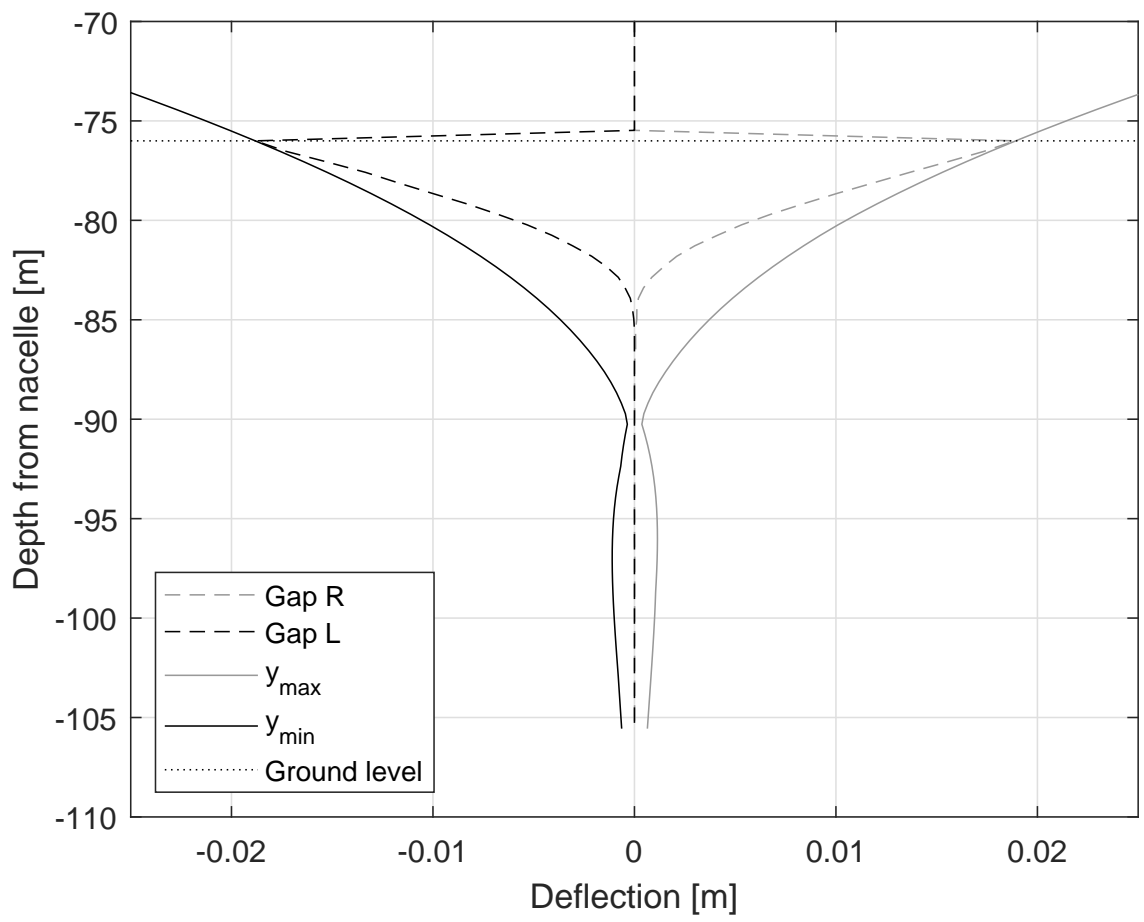
Figure 17: Profile of maximum and minimum deflection of the OWT foundation, and the steady state gap formed on the right and left sides of the pile. The gap is significant to a depth of approximately 85 m
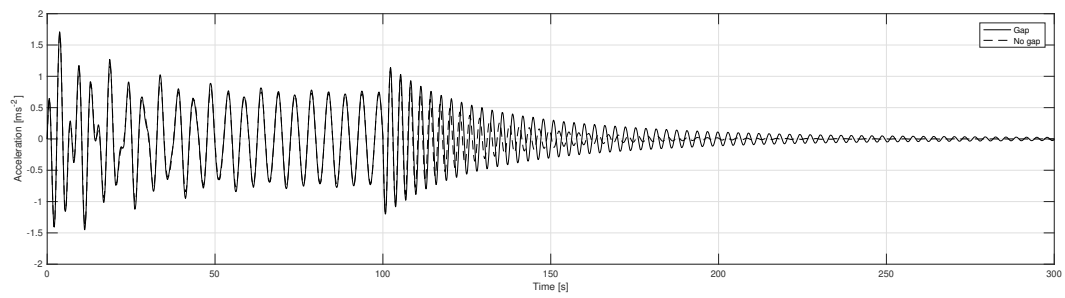
Figure 18: Acceleration time history of the OWT model during a rotor stop simulation. The output of simulations with and without the gapping algorithm are presented